Available online at www.sciencedirect.com
ScienceDirect
Advances in Space Research 44 (2009) 277–307
ADVANCES IN SPACE RESEARCH (a COSPAR publication)
www.elsevier.com/locate/asr

Review

A review of observed variability in the dayside ionosphere of Mars

Paul Withers

Center for Space Physics, Boston University, 725 Commonwealth Avenue, Boston, MA 02215, USA

Received 3 September 2008; received in revised form 3 April 2009; accepted 29 April 2009

Abstract

Recent measurements by Mars Global Surveyor and Mars Express have greatly increased the number of observations of the martian dayside ionosphere available for study. Together with earlier measurements from the Viking era, these datasets have been used to investigate variations in well-known properties of the martian dayside ionosphere and to discover new ionospheric features. The dayside ionosphere includes the main peak, called the M2 layer, and a lower layer, called the M1 layer. In the topside, above the M2 layer, electron densities exponentially decrease with increasing altitude.

The following variations in ionospheric properties are addressed. Peak electron densities and altitudes depend on solar zenith angle as predicted by Chapman theory. Electron densities in the M1 layer have a similar dependence on solar zenith angle. Peak electron densities are sensitive to the Sun's rotation and solar flares, although the quantitative dependence of peak electron densities on solar irradiance is not as strong as theoretically predicted. Peak electron densities are increased in regions of strong and vertical magnetic field, possibly due to a two-stream plasma instability that increases electron temperatures. Peak altitudes follow fixed pressure levels in the neutral atmosphere, rising and sinking in response to thermal tides and dust storms. Electron densities below the M2 layer are highly variable because the relevant portion of the solar spectrum (<20 nm) varies significantly on a range of timescales. In addition, electron densities below the M2 layer increase in response to solar flares, solar energetic particle events, and increases in meteoroid flux. Electron densities above the M2 layer are affected by magnetic fields. Abrupt changes in topside electron density with altitude are sometimes observed above strong magnetic fields and topside electron densities are increased in regions of strong and vertical magnetic field. Layering has been observed at a range of altitudes throughout the topside. A bulge in electron densities is a persistent feature at 160–180 km, whereas layers above 200 km occur sporadically. The upper boundary of the ionosphere is affected by complex interactions with the dynamic solar wind.

In summary, external factors, including the solar irradiance, the solar wind, and meteoroid flux, and internal factors, including neutral atmospheric density and composition, solar zenith angle, and crustal magnetic fields, affect the variability of the martian dayside ionosphere.

Keywords: Mars; Ionosphere; Plasma

1. Background

Mars is currently a major focus of solar system exploration. Recent missions have demonstrated that the martian environment constitutes a tightly coupled system in which the properties and behaviour of one component of the system can influence even the most distant components. This is exemplified by the dayside ionosphere, whose state depends on such disparate phenomena as the solar photon spectrum, the meteoroid flux at Mars, remanent magnetism in ancient crustal rocks, and atmospheric dust storms. In this paper I shall review present knowledge of variability of the martian dayside ionosphere.

Previous reviews of the martian ionosphere include Zhang et al. (1990b), Barth et al. (1992), Shinagawa (1996), Trotignon et al. (2000) and Fox (2004a). These reviews predate the acquisition of extensive datasets by two instruments on Mars Express — the radio occultation

E-mail address: withers@bu.edu

0273-1177/$36.00 © 2009 COSPAR. Published by Elsevier Ltd. All rights reserved.
doi:10.1016/j.asr.2009.04.027

experiment, MaRS, and the topside radar sounder, MARSIS (Pätzold et al., 2005; Gurnett et al., 2005). These Mars Express datasets, and the set of 5600 electron density profiles acquired by the Mars Global Surveyor (MGS) radio occultation experiment in 1998–2005 (Hinson et al., 1999; Hinson et al., 2000; Withers et al., 2008), have provided new stimuli for martian ionospheric studies. The large sizes of these three datasets promote studies of variability in ionospheric properties, including the discovery and characterization of atypical features.

This paper is restricted to the dayside of the martian ionosphere, which has been studied much more than the nightside. The nightside ionosphere has been sampled by fewer types of instruments than the dayside, and those instruments have made fewer measurements on the nightside than they have on the dayside. Also, since plasma densities are smaller on the nightside than on the dayside, a fixed absolute instrumental uncertainty corresponds to a greater relative uncertainty on the nightside than on the dayside. The characteristics of the nightside ionosphere are briefly summarized at the end of Section 2.

Studies of the variability of a system are valuable for understanding that system. Such studies can discover new phenomena and provide challenging tests for theoretical models. They can also determine causal relationships between the observable responses of the system and external stimuli, and elucidate how these causal relationships depend upon the state of the system.

The structure of this paper is as follows. Section 2 contains an introduction to the martian ionosphere, Section 3 discusses Chapman theory, which provides a simple explanation for a range of ionospheric phenomena, and Section 4 describes two types of instruments whose ionospheric measurements have been particularly important. Sections 5–7 discuss variability in, below, and above the main ionospheric layer, respectively. Section 8 considers predicted variations in ionospheric chemistry and electrodynamics, areas for which few pertinent observations have been made.

2. Introduction to the martian ionosphere

Meaningful interpretation of observations of ionospheric variability requires some knowledge of ionospheric processes and properties. This section introduces aspects of the martian ionosphere that will be useful for interpreting the observed variations that are described in subsequent sections.

A planetary ionosphere is strongly influenced by the chemical composition of the relevant neutral atmosphere. The only comprehensive data on the chemical composition of the martian dayside upper atmosphere are from neutral mass spectrometers on the two Viking Landers (Nier and McElroy, 1977). These instruments, whose measurements are shown in Fig. 1, measured vertical profiles of species CO_2, N_2, Ar, CO and O_2 between 120 km and 200 km, but were not capable of measuring O. NO abundances were

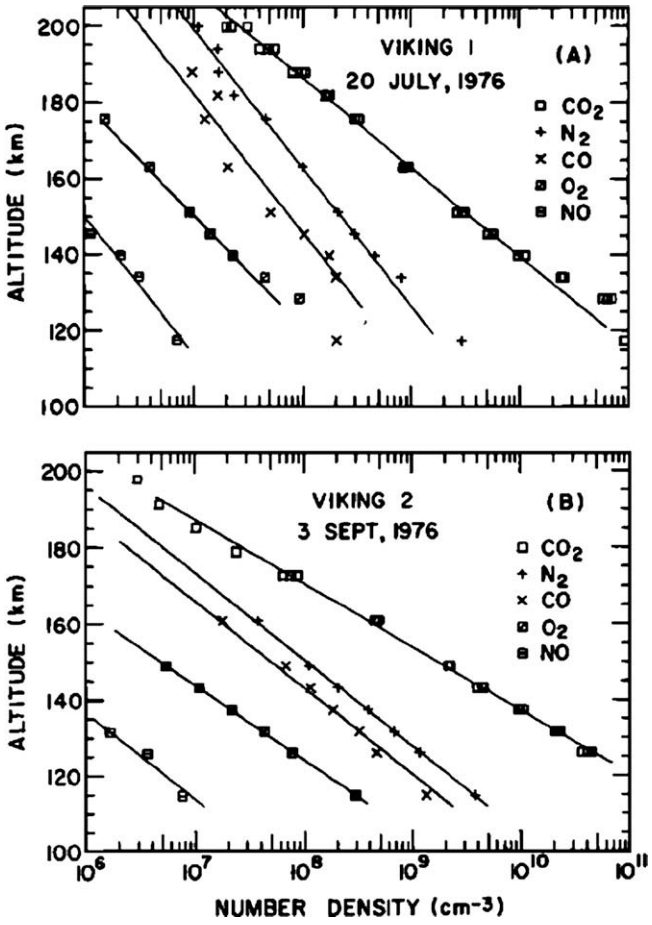

Fig. 1. Number densities of CO_2, N_2, CO, O_2 and NO determined from measurements made by upper atmospheric mass spectrometers on the Viking 1 and 2 Landers. Ar was also measured, but is not shown. These instruments could not measure atomic oxygen, whose presence was inferred from Viking ionospheric data. Reproduced from Fig. 4 of Nier and McElroy (1977). Copyright 1977 American Geophysical Union. Reproduced by permission of American Geophysical Union.

also inferred. CO_2 was the most abundant *measured* species at all altitudes, but ultraviolet remote sensing data and ionospheric composition data strongly imply that O is a major constituent of the upper atmosphere (Chen et al., 1978; Stewart et al., 1992). A neutral atmospheric composition model that includes atomic oxygen was developed from the Viking measurements, and it was discussed in Hanson et al. (1977) and Chen et al. (1978). The O/CO_2 ratio, which is predicted to vary with altitude and local solar time, strongly influences properties of the neutral upper atmosphere and ionosphere, and O is predicted to become more abundant than CO_2 somewhere above 200 km (Bougher et al., 1999).

The ultimate source of most plasma in the martian dayside ionosphere is the photoionization of CO_2 by solar photons at wavelengths shorter than 90 nm (Lide, 1994; Schunk and Nagy, 2000). Photoionization of other species, such as O, is only important at altitudes several scale heights above the main ionospheric peak. Relative to photoionization, influxes of charged particles typically do not

cause substantial impact ionization on the dayside (Kallio and Janhunen, 2001), except possibly during infrequent large solar energetic particle events (Leblanc et al., 2002).

Since plasma is produced by photoionization, the plasma densities depend on the photoionization rate, and the vertical distribution of plasma depends on the vertical distribution of photoionization. The maximum photoionization rate for a given wavelength occurs where the optical depth is unity. Fox and Yeager (2006) calculated this altitude as a function of wavelength for solar zenith angles (SZA) of 60° and 90°, as shown in Fig. 2. The altitude at which optical depth equals unity is approximately uniform for wavelengths between 20 nm and 90 nm, and it is approximately 140 km at SZA = 60°. This lack of dependence on wavelength arises because the ionization cross-section for CO_2 is approximately uniform at 3×10^{-17} cm^2 for these wavelengths (Schunk and Nagy, 2000), and so this portion of the ionizing spectrum can be considered to be effectively monochromatic.

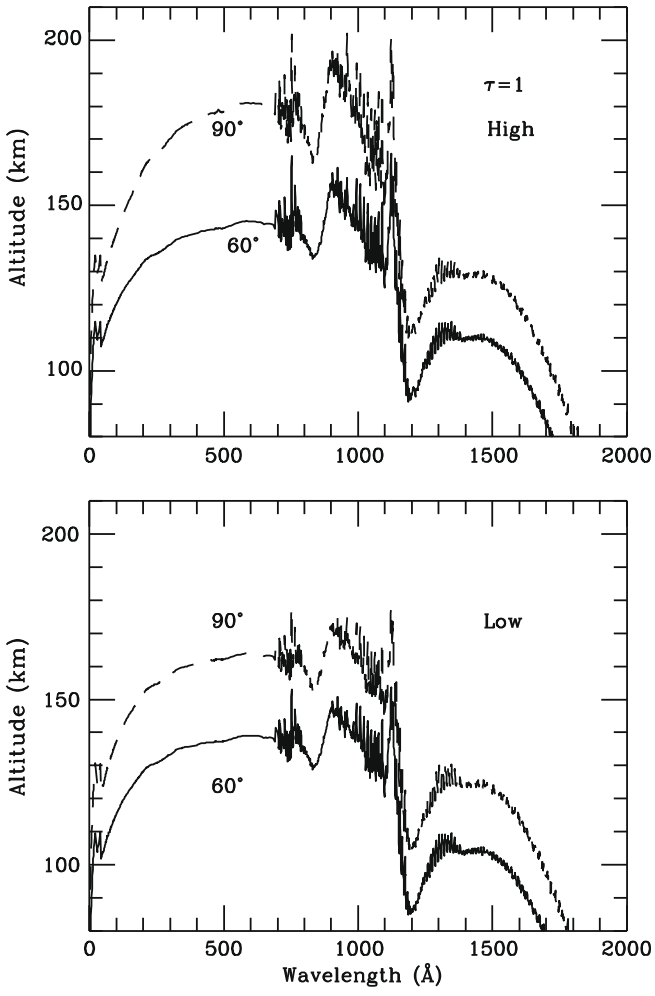

Fig. 2. Predicted altitude at which optical depth equals unity as a function of wavelength. Wavelengths longer than 90 nm do not ionize CO_2. Top (bottom) panel is for high (low) solar activity. Solid (dashed) lines correspond to SZA of 60° (90°). Reproduced from Fig. 2 of Fox and Yeager (2006). Copyright 2006 American Geophysical Union. Reproduced by permission of American Geophysical Union.

At wavelengths shorter than 20 nm, the altitude at which optical depth equals unity decreases as wavelength decreases, reaching 110 km at 5 nm for SZA = 60°. This dependence on wavelength arises because the ionization cross-section for CO_2 decreases to 1×10^{-18} cm^2 at wavelengths of 5 nm (Schunk and Nagy, 2000). The flux of photons emitted from the Sun is about an order of magnitude greater in the 20–90 nm range than at wavelengths below 20 nm, as shown in Fig. 4 of Martinis et al. (2003), so the production of plasma in the martian dayside ionosphere is dominated by 20–90 nm solar irradiance. This wavelength range contains the important He II line at 30.4 nm.

Retarding potential analyzers (RPA) on the two Viking Landers provide the only comprehensive data on the composition of the martian dayside ionosphere (Hanson et al., 1977; Chen et al., 1978). They measured vertical profiles of O_2^+, CO_2^+ and O^+ between 100 km and 300 km, as shown in Fig. 3. The ion composition data are strong evidence for the presence and importance of O in the neutral atmosphere. Although CO_2 is the dominant neutral, O_2^+ is the dominant ion. This is because, to first-order, the only important ionospheric reactions are $CO_2 + h\nu \rightarrow CO_2^+ + e, CO_2^+ + O \overset{fast}{\rightarrow} O_2^+ + CO$ and $O_2^+ + e \overset{slow}{\rightarrow} O + O$. The main loss process is the dissociative recombination of O_2^+. A single dayside ionospheric layer near 140 km, now called the M2 layer, is present in the Viking RPA data (Rishbeth and Mendillo, 2004). The primary source of plasma in the M2 layer is photoionization by solar extreme-ultraviolet (EUV) photons with wavelengths between 20 nm and 90 nm. The observed altitude, width, peak electron density and shape of this layer are broadly consistent with models based on Chapman theory, which is discussed in Section 3 (Chapman, 1931a; Chapman, 1931b; Chen et al., 1978). Note that, in this paper, the "width" of a layer refers to the vertical extent of the layer. Chapman theory includes a simple representation of photochemical processes, but does not include transport processes.

Theories that include photochemical processes, but neglect plasma transport, are sufficient to describe the M2 layer (and below) because timescales for plasma transport processes are much longer than photochemical timescales in (and below) the M2 layer (Schunk and Nagy, 2000; Martinis et al., 2003). The photochemical timescale, τ_{PC}, is $1/(\alpha N)$ and τ_D, the "diffusive time constant", is H^2/D (Rishbeth and Garriott, 1969). The dissociative recombination coefficient, α, equals $1.95 \times 10^{-7}(300\text{ K}/T_e)^{0.70}$ cm^{-3} s^{-1} for $T_e < 1200$ K and $7.38 \times 10^{-8}(1200\text{ K}/T_e)^{0.56}$ cm^{-3} s^{-1} for $T_e > 1200$ K (Schunk and Nagy, 2000). A typical value of α is 2×10^7 cm^{-3} s^{-1}. The electron density, N, rarely exceeds a few times 10^5 cm^{-3} and most existing ionospheric datasets are limited by their uncertainties to densities greater than 10^3 cm^{-3}. The neutral scale height, H, is typically within 50% of 10 km (Withers, 2006). The plasma diffusion coefficient, D, equals $k_B(T_e + T_i)/m_i\nu_{in}$, where k_B is Boltzmann's constant (Rishbeth and Garriott, 1969). The electron temperature, T_e, and ion temperature, T_i, equal the neutral temperature,

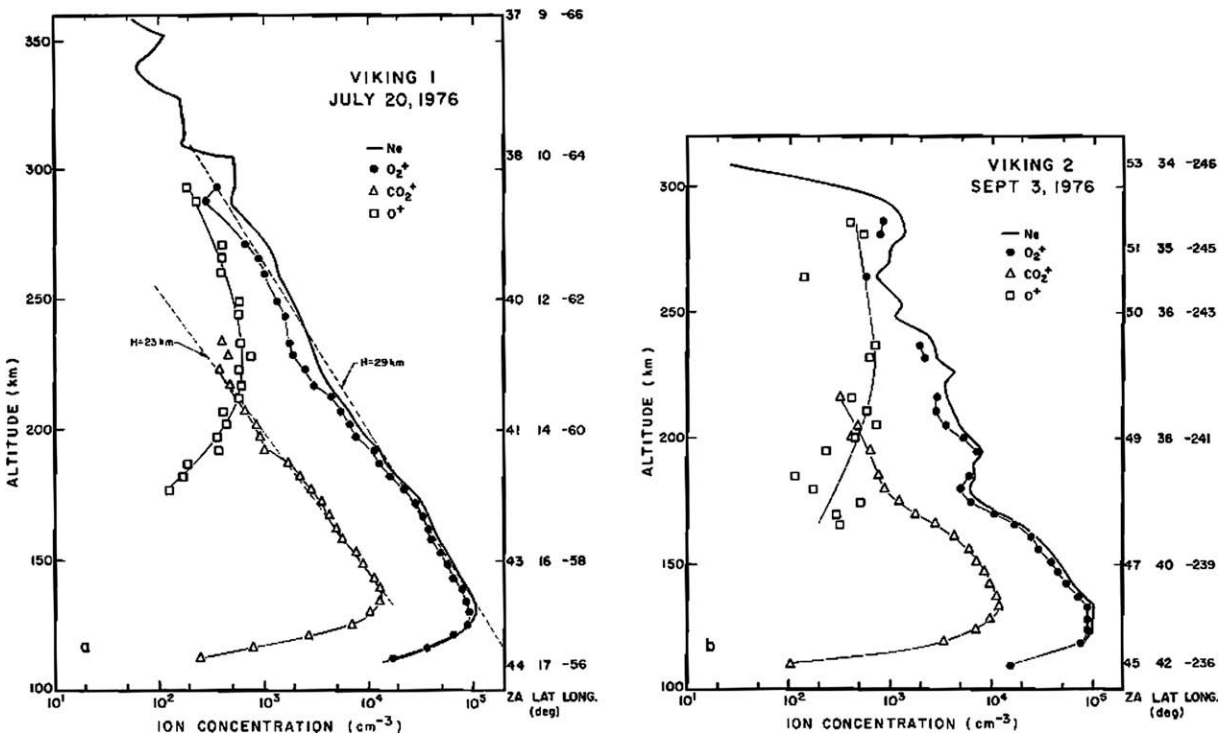

Fig. 3. Concentrations of O_2^+, CO_2^+ and O^+ measured by retarding potential analyzers on the Viking 1 and 2 Landers. The solar zenith angle (degrees), latitude (°N) and longitude (°E) of each lander are shown to the right of each panel as functions of altitude. Reproduced from Fig. 6 of Hanson et al. (1977). Copyright 1977 American Geophysical Union. Reproduced by permission of American Geophysical Union.

T_n, of ≈200 K at 100 km. At higher altitudes, $T_e > T_i > T_n$ and both T_e and T_i exceed 1000 K by 200–250 km (Hanson et al., 1977; Chen et al., 1978; Hanson and Mantas, 1988). The ion mass, m_i, is 32 Da for O_2^+ ions, decreasing with increasing altitude to 16 Da if O^+ ions become most abundant. The ion-neutral collision frequency, ν_{in}, is given by Banks and Kockarts (1973):

$$\nu_{in} = 2.9 \times 10^{-9} \frac{m_n}{m_i + m_n} n_n \sqrt{\frac{\alpha_{pol}}{m_r}} \quad (1)$$

where ν_{in} is in units of s^{-1}, n_n is in units of cm^{-3}, α_{pol} is in units of 10^{-24} cm^3, m_r is in units of daltons, m_n is the mass of the neutral species, n_n is the number density of the neutral species, α_{pol} is the polarizability of the neutral species, and m_r is the reduced mass of the charged and neutral species. For CO_2, α_{pol} is 2.911×10^{-24} cm^3 (Lide, 1994). For O_2^+ ions and CO_2 neutrals, $(\nu_{in}/s^{-1}) \sim 20\ (n_n/3 \times 10^{10}\ cm^{-3})$, where the reference neutral number density of 3×10^{10} cm^{-3} is a typical value for the altitude of the M2 layer at the subsolar point (Section 5.5). For O_2^+ ions, $T_e = T_i = 500$ K, $\nu_{in} = 20$ - s^{-1} and $H = 10$ km, D equals 1.3×10^4 m^2 s^{-1} and τ_D equals 2 h. For $\alpha = 2 \times 10^7$ cm^{-3} s^{-1} and $N = 10^5$ cm^{-3}, τ_{PC} equals 1 min.

Above the M2 layer, τ_{PC} increases exponentially with altitude and τ_D decreases exponentially with altitude. Several scale heights above the peak of the M2 layer, above about 200 km, the diffusive time constant becomes shorter than the photochemical timescale, so transport processes become important and eventually control the structure of the topside of the dayside ionosphere. The photochemical timescale is less than 10 min for plasma densities greater than 8000 cm^{-3}, and the two timescales are on the order of 10 min at the photochemical/transport boundary.

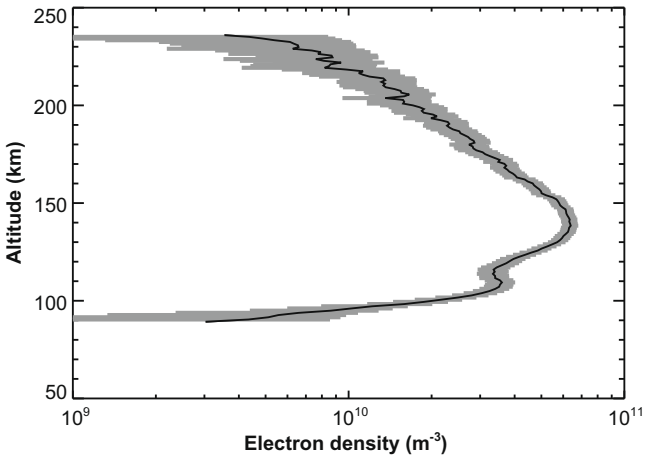

Fig. 4. Profile 0337M41A.EDS, a typical MGS radio occultation electron density profile. It was measured at latitude 66.6°N, longitude 164.3°E, 2.8 h LST, $L_s = 83.9°$ and SZA = 83.0° on 2 December 2000. LST is local solar time and L_s, the areocentric longitude of the Sun, indicates the martian season. L_s is the angle between the Mars-Sun line and the Mars-Sun line at the northern spring equinox. The nominal profile is the solid line and 1σ uncertainties in the electron densities are marked by the grey region. Note the M2 layer at 140 km and the M1 layer at 110 km. Previously published as Fig. 1 of Withers et al. (2008). Copyright 2008 American Geophysical Union. Reproduced by permission of American Geophysical Union.

Thousands of vertical profiles of dayside ionospheric electron density have been obtained by radio occultation experiments, which are discussed further in Section 4 (Mendillo et al., 2003; Pätzold et al., 2005; Withers and Mendillo, 2005). Fig. 4 shows a typical MGS radio occultation electron density profile (Withers et al., 2008). Many dayside electron density profiles have also been obtained by the AIS mode of the MARSIS instrument on Mars Express, which is discussed further in Section 4, as shown in Figs. 5 and 6 (Gurnett et al., 2008). Electron density profiles, which do not provide any information on ion composition, can be interpreted with the support of the Viking measurements of ion and neutral composition. The dayside electron density profiles obtained by radio occultation experiments are dominated by the M2 layer, as were the Viking RPA profiles, although a smaller and more variable layer, called the M1 layer, is also present at lower altitudes (Rishbeth and Mendillo, 2004). Observations of the M1 layer show that it is sometimes a strong local maximum in electron density, and sometimes merely a shoulder or ledge on the bottom of the M2 layer. MARSIS electron density profiles do not extend below the M2 layer, as discussed in Section 4.

Production of the low-altitude M1 layer by photoionization requires photons that are more penetrating than the 20–90 nm photons responsible for the M2 layer; i.e., photons with wavelengths shorter than 20 nm (Martinis et al., 2003). However, even generous estimates of the flux of these short-wavelength photons are too small for photoionization alone to produce observed plasma densities of

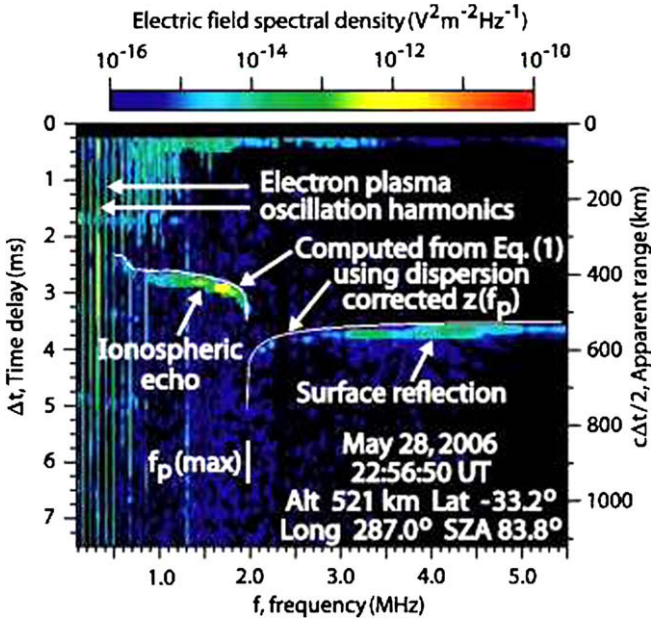

Fig. 5. A MARSIS AIS mode ionogram showing echo intensity as a function of time delay, also called travel time, and frequency. An electron density profile (Fig. 6) was derived from this ionogram. As a consistency check, the white line shows the ionogram trace predicted from the derived electron density profile. "Eq. (1)" refers to Eq. (1) of Gurnett et al. (2008), not of the present work. Reproduced from Fig. 2 of Gurnett et al. (2008). Copyright 2008, with permission from Elsevier.

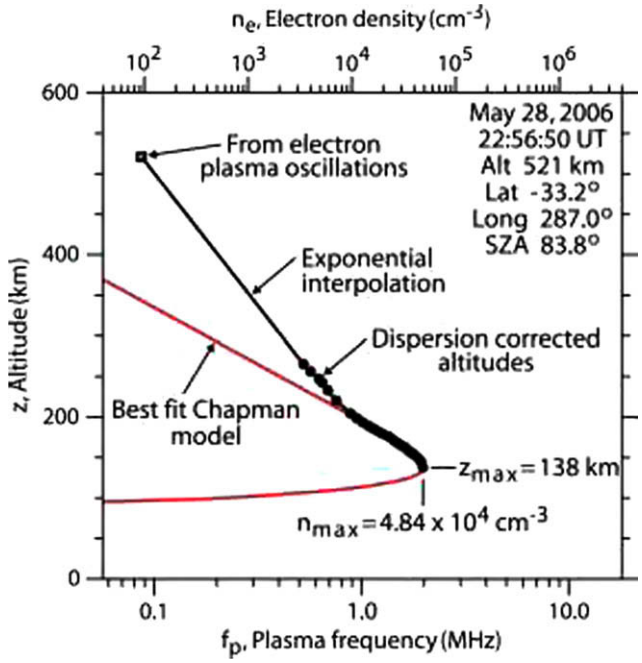

Fig. 6. The black disks show the electron density profile derived from the MARSIS AIS mode ionogram shown in Fig. 5. The red line is a best fit of the data to a Chapman layer. Reproduced from Fig. 3 of Gurnett et al. (2008). Copyright 2008, with permission from Elsevier.

10^4 cm^{-3} at SZA = 60°. Simulations in which photoionization is the only ion production process can produce only a weak shoulder at the altitude of the M1 layer, not a distinct local maximum, even with generous fluxes at short wavelengths (Fox and Yeager, 2006). An additional ion production process, electron impact ionization, is important at the M1 layer (Fox, 2004b). Electron impact ionization is a process whereby energetic photoelectrons ionize neutrals during collisions as they thermalize. Thus the absorption of a single photon can produce more than one ion–electron pair. Since most of the photon energy that exceeds the ionization energy is transferred into kinetic energy of the photoelectron, X-ray photons shortward of 20 nm produce more ion–electron pairs than 20–90 nm EUV photons. Each photon absorbed at the M2 layer produces ~1 ion–electron pair, whereas each photon absorbed at the M1 layer produces ~10 ion–electron pairs (Fox and Yeager, 2006). This "turbo-charger" effect is responsible for the M1 layer being a distinct layer and sometime local maximum in plasma density, rather than a mere shoulder on the bottomside of the M2 layer.

Above the M2 layer, electron densities fall off exponentially with altitude. Their scale height is typically 30–40 km (Kliore, 1992). This relatively small scale height has been interpreted as evidence for the presence of horizontal magnetic fields that impede vertical motion of plasma (Hanson and Mantas, 1988; Shinagawa and Cravens, 1989; Shinagawa and Cravens, 1992). The question of whether these fields are intrinsic or induced was intensely debated after the Viking missions until the arrival at Mars of the MGS magnetometer. The thermal pressure in the martian iono-

sphere rarely exceeds the solar wind dynamic pressure (Shinagawa and Cravens, 1989 and references therein). Consequently, pressure balance requires either that the ionospheric thermal pressure is augmented by the magnetic pressure of an intrinsic field generated within the solid body of the planet or that the solar wind magnetic field piles up into the ionosphere, instead of standing off at an ionopause, and drapes around the planet (Crider et al., 2002; Bertucci et al., 2003). Most pre-MGS analyses favoured the latter scenario, concluding that the intrinsic field, if present at all, is small in comparison to the induced field and that the interaction with the solar wind induces a horizontal magnetic field of about 50 nT throughout the dayside ionosphere (Shinagawa and Cravens, 1992; Nagy et al., 2004 and references therein).

The MGS magnetometer discovered that Mars does not have a strong global magnetic field capable of holding off the solar wind, yet it possesses localized regions of strong magnetic fields generated by remanent magnetism in its crust (Acuña et al., 1999; Acuña et al., 2001). In certain locations, the magnetic field strength at ionospheric altitudes can exceed 1000 nT, as shown in Fig. 10 of Brain et al. (2003). Elsewhere, crustal fields are weak or absent. These localized regions of strong field produce unusual magnetic topologies. Magnetic fieldlines can rotate from vertical to horizontal over distances of a few hundred kilometres, a fraction of the planetary radius. Mini-magnetospheres are formed where closed and strong fieldlines isolate ionospheric plasma from solar wind plasma. Cusp-like conditions prevail on their boundaries, which permit solar wind plasma to flow downwards into the ionosphere easily and ionospheric plasma to flow outwards easily (Brain et al., 2007).

The induced magnetic field caused by the interaction of the solar wind with the ionosphere is variable with SZA and solar wind pressure. Pre-MGS expectations for horizontal fields of approximately 50 nT at the subsolar point during typical solar wind dynamic pressures of 1 nPa were confirmed by the MGS magnetometer (Brain et al., 2003). The magnitude of the induced magnetic field is proportional to the square root of the solar wind dynamic pressure (Crider et al., 2003). For solar wind dynamic pressures of 0.25–4 nPa, the magnitude of the induced magnetic field at the subsolar point varies between 25 nT and 100 nT. The magnitude of the horizontal component of the induced magnetic field decreases linearly from its subsolar value to 5 nT as SZA increases from 0° to 180°, as shown in Fig. 7 (Brain et al., 2003). The magnitude of the vertical component of the induced magnetic field is a few nT for all SZAs. A wide range of theoretical simulations have investigated the interaction of the solar wind and the martian ionosphere (e.g., Ma et al., 2004; Brecht and Ledvina, 2006; Harnett and Winglee, 2006; Kallio et al., 2006; Kaneda et al., 2007). The magnetic environment of Mars is unusual, possibly unique in the solar system.

To conclude this section, I briefly address the nightside ionosphere of Mars, which was not probed by the Viking

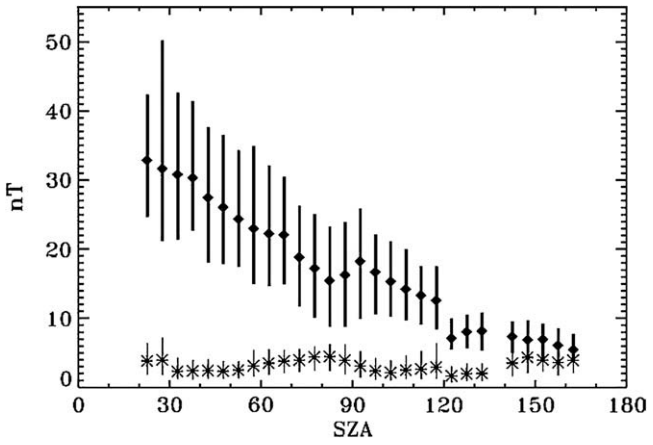

Fig. 7. The magnitude in nT of the median horizontal field (diamonds) at MGS mapping altitudes (380–420 km) is shown as a function of solar zenith angle (degrees), along with radial field magnitude (asterisks). Vertical error bars denote quartiles around the median. Crustal effects are minimized by only including data from 1 degree longitude/latitude bins where the average field magnitude is less than 10 nT when MGS was in the planetary shadow. Reproduced from Fig. 7 of Brain et al. (2003). Copyright 2003 American Geophysical Union. Reproduced by permission of American Geophysical Union.

Landers. Consequently, no measurements of neutral composition, ion composition, ion temperatures, or electron temperatures are available from the nightside. It is important to note that the nightside ionosphere does not begin at SZA = 90° — altitudes above 120 km are sunlit until SZA = 105° or greater. An analysis of Viking radio occultation profiles between SZA = 90° and 125° concluded that ionospheric plasma was only detected in 60% of the profiles (Zhang et al., 1990a). The average of the detected peak electron densities was $5 \times 10^3\ \mathrm{cm}^{-3}$ and the altitudes of the detected peaks were ≈150 km. Nightside electron density profiles from the MGS and Mars Express radio occultation experiments have not yet been published. MARSIS measurements of the nightside ionosphere have found patchy, irregular structures that are possibly similar to nightside holes in ionosphere of Venus (Gurnett et al., 2008). Some of the peak electron densities measured by MARSIS at SZA = 110° exceeded $10^4\ \mathrm{cm}^{-3}$, so relatively high concentrations of plasma can exist on the nightside. Possible sources of nightside plasma include the transport of plasma from the dayside and ionization by precipitating electrons (e.g., Fox et al., 1993; Gurnett et al., 2008). In summary, observations to date suggest that the nightside ionosphere is highly variable, although causes and effects are not well identified and models are not well validated.

3. Chapman theory

Many aspects of the martian dayside ionosphere, particularly properties of the M2 layer, can be explained by simple Chapman theory (Chapman, 1931a; Chapman, 1931b; Rishbeth and Garriott, 1969; Chamberlain and Hunten, 1987). As the predictions of this theory are frequently used in the literature to interpret observations of martian iono-

spheric variability, I now introduce the central results of this theory before discussing its specific application at Mars in subsequent sections. The pertinent point is not whether Chapman theory provides a complete and accurate description of the state of the ionosphere, but rather whether Chapman theory accurately predicts the dependence of certain ionospheric characteristics on external and internal factors.

Why is Chapman theory commonly applied to Mars even though Chapman theory offers a woefully inadequate description of the terrestrial ionosphere and makes many simplifying assumptions that are not wholly valid for any ionosphere? Perhaps the two main reasons for this are as follows. (A) The vertical shape of martian ionospheric profiles can be fit impressively well by a Chapman function. In particular, the shapes of profiles obtained by the Mars Express radio occultation experiment, which have significantly smaller uncertainties than earlier experiments, are extremely well represented by Chapman functions from a scale height below to several scale heights above the M2 peak. This vertical extent contains well over half the plasma in the entire ionosphere. (B) It is prohibitively time-consuming to fit more sophisticated models to thousands of radio occultation profiles and thousands of MARSIS profiles. The probability that a research effort will use Chapman theory seems to increase as the number of observations considered in the research effort increases from one (Viking 1 RPA dataset) to two (Viking 1 and 2 RPA datasets) to many (recent radio occultation and MARSIS observations). Investigation of how many parameters must be included in a sophisticated photochemical model of the ionosphere before the agreement between predictions and observations near the M2 peak is significantly better than that offered by the three parameters of a Chapman layer, and of how tightly the observations constrain the assumed values of the parameters, might be illuminating.

Some of the differences between Mars and Earth that might explain why the vertical profile of the martian ionosphere has this simple shape are as follows. (A) Only one neutral species, the most abundant one, CO_2, is important for the absorption of EUV photons in the martian atmosphere, unlike the mixture of O, O_2 and N_2 on Earth. (B) The cross-section for the absorption of ionizing photons by neutral molecules does not vary greatly with altitude or wavelength in the EUV region on Mars, unlike Earth. (C) Most plasma in the martian ionosphere is produced and destroyed by the same single photoionization step, single charge exchange step, and single dissociative recombination step, as outlined in Section 2. (D) Only molecular ions, and only a single species of molecular ion $\left(O_2^+\right)$, are important near the main peak of the martian ionosphere, unlike the mixture of atomic (O^+) and multiple molecular ions $\left(O_2^+, NO^+\right)$ found on Earth. (E) Plasma transport processes are negligible near the main peak of the martian ionosphere, unlike Earth.

There are several sub-divisions of Chapman theory and, since O_2^+ is the most abundant ion in the martian dayside ionosphere and its primary loss process is dissociative recombination with an electron, the appropriate one for Mars concerns molecular ions whose loss rate is proportional to the square of the electron density.

In this theory, the electron density, N, depends on altitude, z, as follows:

$$N = N_0 \exp\left(\frac{1}{2}\left(1 - \frac{z - z_0}{H} - Ch \exp\left(-\frac{z - z_0}{H}\right)\right)\right) \tag{2}$$

where N_0 is the peak electron density above the subsolar point, z_0 is the altitude at which N equals N_0, H is the scale height of the neutral atmosphere, Ch is a dimensionless geometrical correction factor that reduces to sec(SZA) for sufficiently small values of SZA, and SZA is solar zenith angle. Equivalently,

$$N = N_m \exp\left(\frac{1}{2}\left(1 - \frac{z - z_m}{H} - \exp\left(-\frac{z - z_m}{H}\right)\right)\right) \tag{3}$$

where z_m and N_m satisfy:

$$N_m = \frac{N_0}{\sqrt{Ch}} \tag{4}$$

$$z_m = z_0 + H \ln Ch \tag{5}$$

$N(z)$ for a Chapman layer is shown in Fig. 8. N_m is the peak electron density at a given SZA and z_m is the altitude at which N at this SZA equals N_m. According to Eq. (3), $N(z)$ is completely defined by three parameters: N_m, z_m and H. Eq. (3) can also be used to show that the full width at half maximum of $N(z)$ is $3.6H$ and the total electron content is $4.13N_mH$.

The altitude z_m is a function of SZA because it corresponds to a slant optical thickness of unity. The altitude z_m increases with increasing SZA, although $z_m - z_0$ is less than $0.5H$ for SZA $< 52°$ and less than H for SZA $< 68°$ (Eq. (5)). A given optical thickness occurs at higher altitude if the Sun is close to the horizon than if it is near zenith because solar photons must propagate

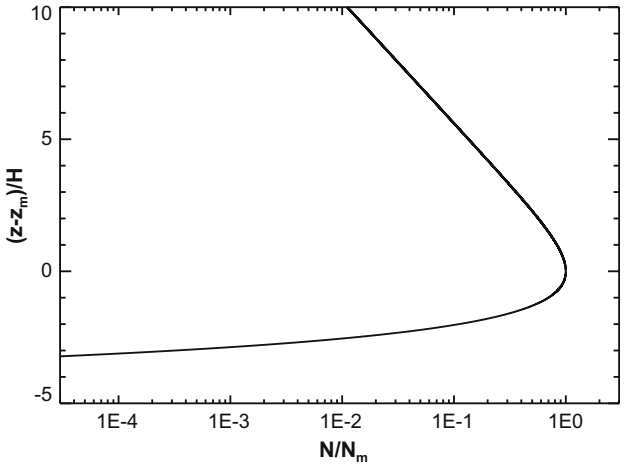

Fig. 8. Electron density, N, as a function of altitude, z, from Eq. (3). N_m is the peak electron density, z_m is the altitude at which $N = N_m$, and H is the neutral scale height.

through a volume of space containing more molecules per unit area of wavefront to descend a given vertical distance. The peak electron density, N_m, is a function of SZA because the peak ion production rate is. The peak ion production rate varies with SZA, even though the ionizing flux at optical depth of unity is constant at $1/e$ times its initial value, because the neutral number density at optical thickness of unity varies with SZA (Chamberlain and Hunten, 1987). Since z_m increases as SZA increases, the neutral number density at an optical depth of unity decreases, which causes the peak ion production rate and N_m to decrease. According to Eq. (4), N_m is proportional to Ch raised to the power -0.5, which reduces to the cosine of SZA raised to the power 0.5 for SZAs that are not close to the terminator. The altitudes z_0, which corresponds to a vertical optical depth of unity, and z_m satisfy:

$$\sigma n(z_0)H = 1 \tag{6}$$

$$\sigma n(z_m)HCh = 1 \tag{7}$$

where σ is the ionization cross-section and n is neutral number density. The subsolar peak electron density, N_0, satisfies:

$$N_0^2 = \frac{F}{\alpha e H} \tag{8}$$

where F is the ionizing flux at the top of the atmosphere, α is the dissociative recombination coefficient for the appropriate molecular ion and e is 2.71828.... Hence N_0 and N_m are proportional to the square root of F. Note also that N_0 and N_m depend on the neutral scale height, H. The dissociative recombination coefficient, α, depends on the ion species. For O_2^+ on Mars and many other molecular species, α also depends on electron temperature (Schunk and Nagy, 2000).

For $|z - z_m|/H \ll 1$, Eq. (3) reduces to:

$$N = N_m\left(1 - \left(\frac{z - z_m}{2H}\right)^2\right) \tag{9}$$

Data can be fitted to Eq. (3), and approximations to it like Eq. (9), to determine best-fit values of N_m, z_m and H (e.g., Withers and Mendillo, 2005). Eq. (9) can be used in a standard linear least-squares fitting approach, whereas Eq. (3) cannot (Bevington, 1969). However, Eq. (9) is an approximation that is only valid within a narrow range centred on z_m, whereas Eq. (3) is not an approximation. Consequently, two groups may report somewhat different best-fit values even when fitting the same set of measurements if they use different Chapman-derived fitting functions or perform their fits using data points selected from different vertical ranges.

As shown in Fig. 8, N increases monotonically with increasing altitude below z_m and decreases monotonically with increasing altitude above z_m. At low altitudes, N increases extremely rapidly with increasing altitude. At high altitudes, Eq. (3) reduces to:

$$N = N_m \exp(1/2) \exp\left(\frac{-(z - z_m)}{2H}\right) \tag{10}$$

At high altitudes N is an exponential function of altitude with a scale height that is twice the neutral scale height.

Several conditions must be satisfied for this theory to be a realistic representation of a planetary ionosphere (Chamberlain and Hunten, 1987). The most significant are that plasma transport processes are negligible and the absorption of ionizing radiation is well characterized by a single cross-section.

Some of the results outlined in this section are generally applicable to any ionospheric region that is controlled by photochemical, not transport, processes, not just those that satisfy the conditions of Chapman theory. The ion production rate in an ionospheric region that is controlled by photochemical processes should, from basic geometric considerations, be proportional to cos(SZA). If ions are primarily produced in photoionization events, then the ion production rate should also be proportional to the ionizing flux, F. If the dominant ion loss process in this region is the dissociative recombination of molecular ions, then the peak electron density should be proportional to $\cos^{0.5}$(SZA) and proportional to $\sqrt{F}$. These relationships will be investigated in the subsequent sections. Those involving the solar zenith angle are easier to test than those involving the ionizing flux because the value of SZA can be easily determined, whereas the appropriate value of F is more challenging to find. Although the concept of a single ionizing flux is useful for developing theory, it is not a well-defined measurable quantity.

Although it serves as a useful representation for Mars, Chapman theory is only a first-order approximation to the real state of the dayside ionosphere. The dayside ionosphere in and below the M2 layer is affected by a wider range of photochemical production and loss processes than are included in Chapman theory. At higher altitudes, transport processes neglected in Chapman theory affect the state of the dayside ionosphere. More sophisticated models are essential theoretical tools (e.g., Martinis et al., 2003; Ma et al., 2004; Fox and Yeager, 2006).

4. Measurement techniques

Most of the measurements discussed in Sections 5–7 were obtained by two types of instruments. The first type are radio occultation instruments. Many such instruments have operated at Mars. Thorough descriptions of this measurement technique and its martian results can be found in, e.g., Tyler et al. (1992), Hinson et al. (1999), Hinson et al. (2000), Tyler et al. (2001) and Mendillo et al. (2003). Radio occultation experiments measure ionospheric properties when the spacecraft passes behind the disk of Mars as viewed from the Earth. At such times, the radio signal between the spacecraft and Earth passes through the atmosphere and ionosphere of

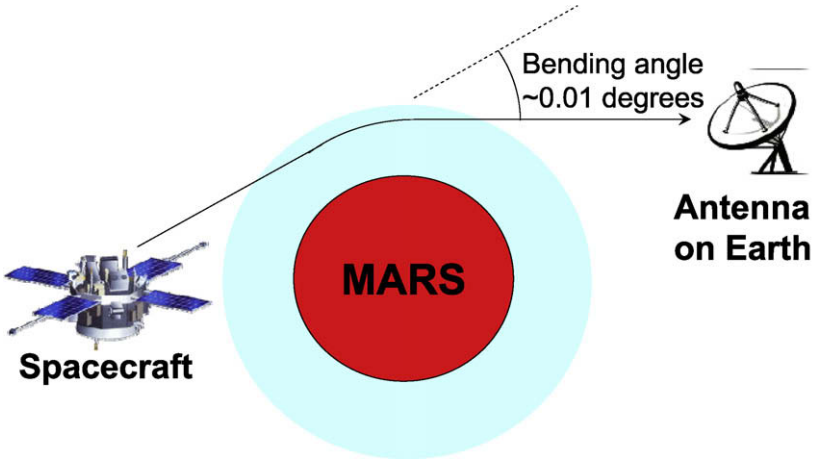

Fig. 9. Illustration of a radio occultation. The line of sight between the spacecraft and Earth passes through the atmosphere and ionosphere of Mars. Refraction in the atmosphere and ionosphere bends the ray path slightly (Hinson et al., 1999; Hinson et al., 2000), which leads to a measurable shift in the received frequency. Atmospheric and ionospheric properties can be derived from the frequency shift.

Mars, as illustrated in Fig. 9. Refraction in the atmosphere and ionosphere bends the ray path slightly, which leads to a measurable shift in the received frequency, from which atmospheric and ionospheric properties can be determined (e.g., Fjeldbo et al., 1971). However, geometric constraints limit such observations to SZAs of 44° to 136° (Gurnett et al., 2008). Martian radio occultation experiments typically use frequencies of a few GHz and wavelengths of a few cm, and their typical ionospheric data products are vertical profiles of electron density between approximately 80 km and 250 km altitude. These profiles typically have vertical resolution of 1 km and uncertainties in electron density on the order of (1–3) $\times 10^3\,\mathrm{cm}^{-3}$. Several hundred electron density profiles were measured by radio occultation experiments before MGS (Mendillo et al., 2003), a small number in comparison to the 5600 measured by the MGS radio occultation experiment. Obtaining electron density profiles from radio occultation measurements requires the assumption that the ionosphere is spherically symmetric. In practice, martian radio occultation measurements are sensitive to ionospheric plasma within about 200 km of the centre of the measurement, so the assumption of spherical symmetry need only be valid over this restricted region (Hinson et al., 1999; Hinson et al., 2000). Note, however that the ionosphere may vary on such horizontal scales near the terminator or above crustal magnetic fields.

The second type are topside radar sounder instruments, of which only the MARSIS instrument on Mars Express has operated at Mars (Picardi et al., 2004; Gurnett et al., 2005; Gurnett et al., 2008). MARSIS transmits radio waves from 0.1 to 5.4 MHz which interact with the ionosphere below the spacecraft, and are then recorded upon their return to the spacecraft. Radio waves can be reflected by the ionosphere and the planetary surface, as shown in Fig. 10. The interaction of radio waves with ionospheric plasma is controlled by the plasma frequency, f_p, which is defined by:

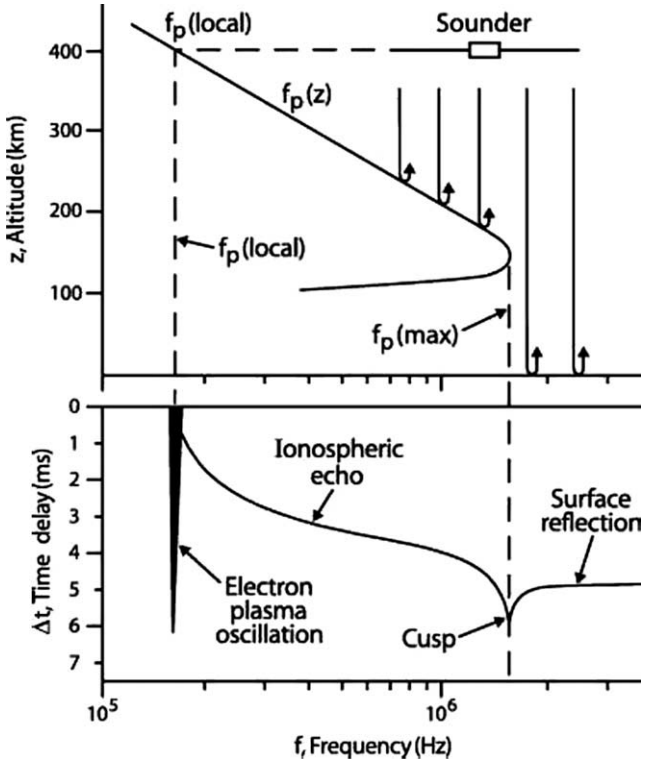

Fig. 10. The top panel shows a representative profile of the electron plasma frequency, f_p, in the martian ionosphere, and the bottom panel shows the corresponding ionogram, which is a plot of the time delay, Δt, for a sounder pulse of frequency f to reflect from the ionosphere/surface and return to the spacecraft. Reproduced from Fig. 1 of Gurnett et al. (2008). Copyright 2008, with permission from Elsevier.

$$f_p^2 = \frac{Ne^2}{4\pi^2\epsilon_0 m_e} \tag{11}$$

where N is electron density, $-e$ is the charge on an electron, ϵ_0 is the permittivity of free space, and m_e is the electron mass. Equivalently,

$$f_p(Hz) = 8979\sqrt{N(cm^{-3})} \tag{12}$$

An electron density of 2×10^5 cm^{-3} corresponds to a plasma frequency of 4 MHz. Radio waves propagate through plasma whose plasma frequency is less than the radio frequency, but are reflected when they encounter plasma whose plasma frequency equals the radio frequency (Rishbeth and Garriott, 1969). MARSIS has two modes, an AIS mode that is optimized for ionospheric observations and an SS mode that is optimized for subsurface observations. When operated in the AIS mode, the instrument transmits a pulse of radio waves at a defined frequency, then records the strength of the reflected signal as a function of time (Gurnett et al., 2008). This is repeated for multiple frequencies between 0.1 MHz and 5.4 MHz. The strength of the reflected signal is usually clearly peaked at one time, which is called the travel time for that frequency. It is straight-forward to determine the peak electron density directly below the spacecraft from a series of travel times as a function of frequency.

It is also possible to determine the vertical profile of electron density between the spacecraft (whose altitude during MARSIS operations is typically between 275 km and 1200 km) and the maximum electron density (whose altitude is variable, but on the order of 130 km) (Nielsen et al., 2006; Morgan et al., 2008). Electron density profiles determined by MARSIS do not extend below the M2 layer. However, this inversion process assumes that plasma densities decrease monotonically with increasing altitude which, although a reasonable approximation, is not always true. The derived vertical electron density profile also depends on assumptions about topside plasma densities between the spacecraft and the closest, or highest altitude, detectable plasma. The smallest plasma density measurable by MARSIS is theoretically 120 cm^{-3}, but, in practice, limitations on the power radiated at low frequencies increase that threshold to the order of 10^4 cm^{-3}, which typically occurs near 200 km altitude (Nielsen et al., 2006; Morgan et al., 2008). Gurnett et al. (2008) described how different topside assumptions can cause the derived altitude of the M2 layer to vary by 10 km and the derived neutral scale height, which is inferred from the width of the M2 layer, to vary by 8 km. These large uncertainties should be considered carefully when MARSIS electron density profiles and their associated higher-level data products are interpreted. Peak electron densities are not sensitive to these assumptions.

5. Variability in the M2 layer

The M2 layer is the easiest ionospheric region to observe. Its properties are photochemically controlled and simple theory explains many of its characteristics. Nonetheless, the M2 layer is affected by variations in SZA, solar irradiance, magnetic field strength, direction and topology, and neutral atmospheric densities. Variations in solar irradiance are caused by the solar cycle, solar rotation, and solar flares. Variations in neutral atmospheric density are caused by thermal tides and atmospheric dust storms. The M2 layer has also been described by Fox and Yeager (2006).

5.1. Peak electron density and SZA

Peak electron density, N_m, varies with SZA. As shown in Fig. 11, Hantsch and Bauer (1990) used radio occultation data, which are restricted to SZA $> 44°$, acquired prior to the MGS mission to find that peak electron density is proportional to cos(SZA) raised to the power 0.57. A similar analysis of MGS radio occultation data found an exponent of 0.42 for low solar activity, 0.465 ± 0.010 for moderate solar activity, and 0.49 for high solar activity (Fox and Yeager, 2006). As shown in Fig. 12, Nielsen et al. (2006) used MARSIS AIS mode data, which extend from the subsolar point to the terminator, to find that peak electron density is proportional to cos(SZA) raised to the power 0.476. Several other data analysis efforts have concluded that peak electron density is proportional to cos(SZA) raised to the power 0.5, as expected from Chapman theory (Gurnett et al., 2005; Gurnett et al., 2008; Withers and Mendillo, 2005; Morgan et al., 2008). However, as discussed by Fox and Yeager (2006), the expected value of the power to which cos(SZA) is raised decreases below 0.5 as the terminator is approached and the approximation of Ch by sec(SZA) becomes less accurate (Eq. (4)). This results from the inadequacies of plane-parallel geometry close to the terminator. The peak electron density is expected to remain proportional to $Ch^{-0.5}$ as the terminator is approached.

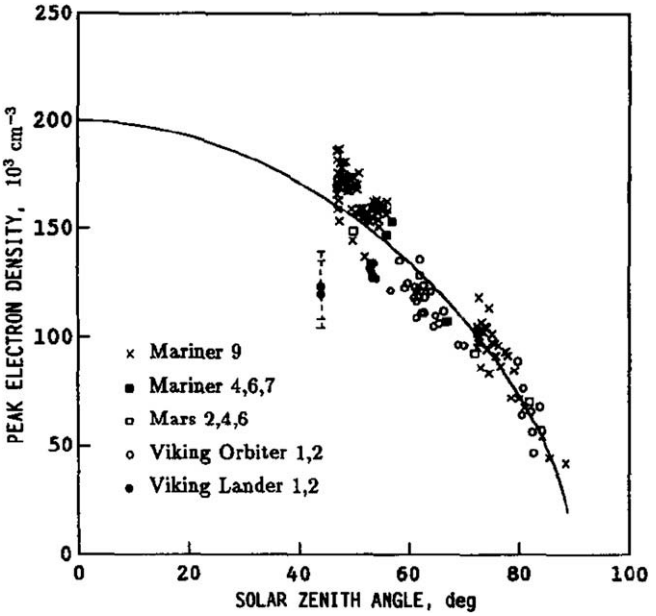

Fig. 11. Measurements of peak electron density, N_m, as a function of SZA. Data from different missions are indicated by different symbols. With two exceptions, the data points were acquired by radio occultation experiments. The two exceptions are the Viking Lander *in situ* retarding potential analyzer data. The solid line is the best fit of the data to a function of the form $N_m = N_0 \cos^n(SZA)$. The fitted subsolar peak electron density, N_0, is 2×10^5 cm^{-3} and the fitted value of the exponent n is 0.57. Reproduced from Fig. 1 of Hantsch and Bauer (1990). Copyright 1990, with permission from Elsevier.

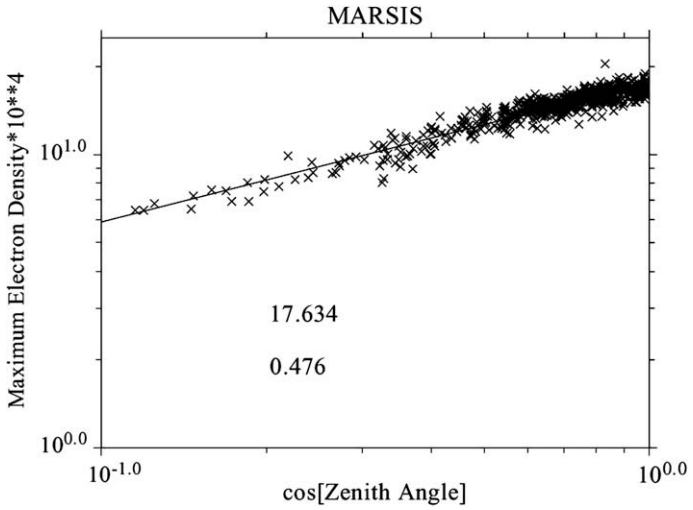

Fig. 12. MARSIS AIS mode measurements of maximum (or peak) electron density, N_m, in units of cm^{-3} as a function of the cosine of SZA (crosses). Data were acquired between July and October 2005. The solid line is the best fit of the data to a function of the form $N_m = N_0 \cos^n(SZA)$. The fitted subsolar peak electron density, N_0, is $1.7634 \times 10^5\ cm^{-3}$ and the fitted value of the exponent n is 0.476. Reproduced from Fig. 2 of Nielsen et al. (2006). With kind permission of Springer Science and Business Media: Fig. 2 of Nielsen et al. (2006).

5.2. Value of subsolar peak electron density

The subsolar peak electron density, N_0, has been characterized in several publications. Safaeinili et al. (2007) used the SS mode of the MARSIS instrument to determine the ionospheric total electron content (TEC) and higher-order moments of the electron density profile as functions of SZA. They then fitted these measurements to a Chapman model for the dependence of electron density on altitude and SZA in order to determine the subsolar peak electron density and neutral scale height The mean subsolar peak electron density found by Safaeinili et al. (2007) was $(2.1 \pm 0.6) \times 10^5\ cm^{-3}$. Measurements of N_m as a function of SZA can be fitted to Eq. (4) to find subsolar peak electron density, N_0. Applying this approach to MARSIS AIS mode data, Nielsen et al. (2006), Gurnett et al. (2008) and Morgan et al. (2008) found $N_0 = 1.79 \times 10^5\ cm^{-3}$, $1.98 \times 10^5\ cm^{-3}$ and $1.58 \times 10^5\ cm^{-3}$, respectively. The results of Nielsen et al. (2006) and Morgan et al. (2008) are shown in Figs. 12 and 13, respectively. More data were available for use in the later publications, which explains some of the variance in these solutions for N_0. Differences in sample size are not the sole explanation, however. For instance, Gurnett et al. (2008) qualitatively estimated N_0, but did not quantitatively fit their data to a model. As shown in Fig. 11, Hantsch and Bauer (1990) applied this method to radio occultation measurements of N_m, which are restricted to SZA > 44°, to find that the best fit subsolar peak electron density was $2.0 \times 10^5\ cm^{-3}$. These values of N_0 are consistent with theoretical predictions based upon Eq. (8) (Withers and Mendillo, 2005).

5.3. Peak electron density and solar irradiance

Many workers have found that peak electron density increases as solar ionizing flux increases. As shown in

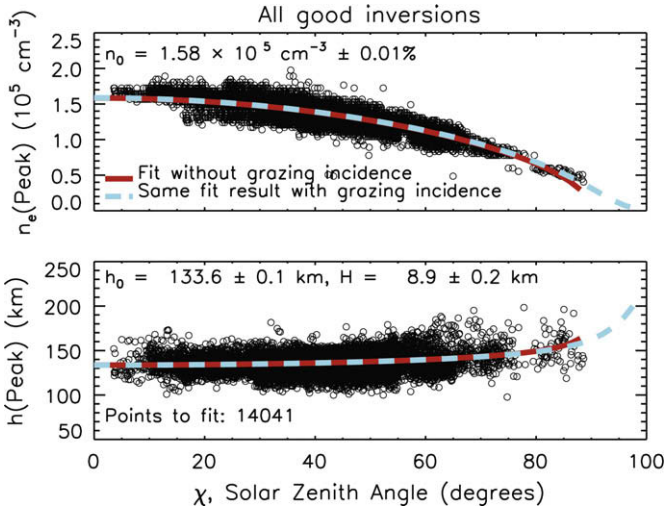

Fig. 13. (Top) MARSIS AIS mode measurements of peak electron densities, N_m, are shown as open circles as a function of SZA. Over 10,000 data points from 14 August 2005 to 31 July 2007 are shown. The solid red line shows the best fit of data that satisfy SZA < 85° to $N_0 = N_m \cos^{0.5}(SZA)$ and the dashed turquoise line shows the best fit of the data to $N_0 = N_m\ Ch^{-0.5}$ (Eq. (4)). The red line's best-fit value of N_0 is $1.58 \times 10^5\ cm^{-3}$. (Bottom) Corresponding peak altitudes, z_m, are shown as open circles. The solid red line shows the best fit of data that satisfy SZA < 85° to $z_m = z_0 + H \ln \sec(SZA)$ and the dashed turquoise line shows the best fit of the data to $z_m = z_0 + H \ln Ch$ (Eq. (5)). The red line's best-fit values of z_0 and H are 133.6 ± 0.1 km and 8.9 ± 0.2 km, respectively. Reproduced from Fig. 4 of Morgan et al. (2008). Copyright 2008 American Geophysical Union. Reproduced by permission of American Geophysical Union. (For interpretation of colour mentioned in this figure caption the reader is referred to the web version of the article.)

Fig. 14, Hantsch and Bauer (1990) used radio occultation measurements of the dependence of N_m on SZA, which are restricted to SZA > 44°, to find that subsolar peak electron density, N_0, varies from $1.5 \times 10^5\ cm^{-3}$ at low solar activity to $2.5 \times 10^5\ cm^{-3}$ at high solar activity. There are no direct measurements of solar ionizing flux at Mars, so

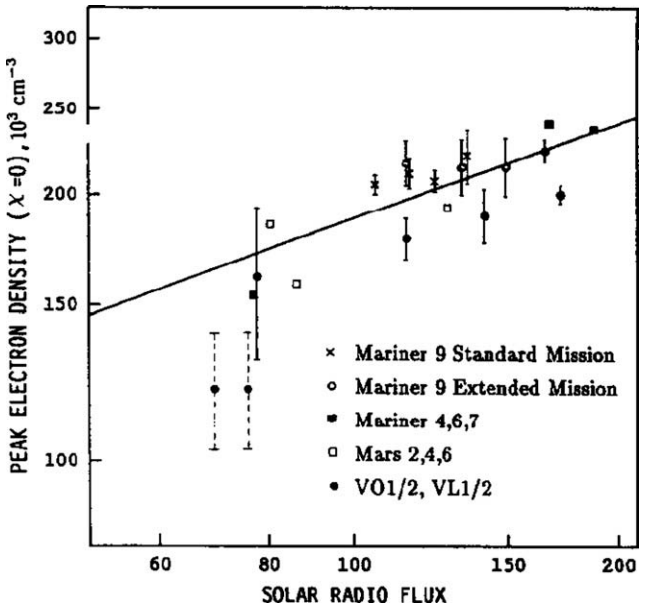

Fig. 14. Inferred subsolar peak electron densities as function of solar radio flux, or $F_{10.7}$, at Earth. Data from different missions are indicated by different symbols. With two exceptions, the data points were acquired by radio occultation experiments. The two exceptions are the Viking Lander *in situ* retarding potential analyzer data. Error bars on Viking Orbiter (Lander) data are shown by vertical solid (dashed) lines. The diagonal solid line is the best fit of the radio occultation data points to a function of the form $N_0 \propto F_{10.7}^k$. The fitted value of this exponent k is 0.36. The subsolar peak electron density varies from $1.5 \times 10^5\ \mathrm{cm}^{-3}$ at low solar activity to $2.5 \times 10^5\ \mathrm{cm}^{-3}$ at high solar activity. Reproduced from Fig. 4 of Hantsch and Bauer (1990). Copyright 1990, with permission from Elsevier.

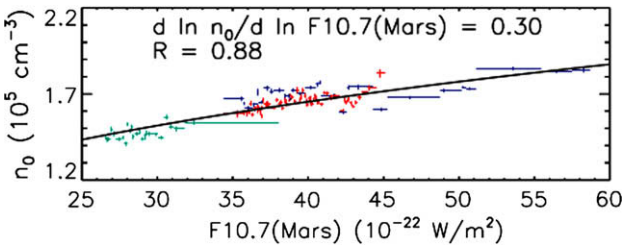

Fig. 15. Subsolar peak electron density, N_0, found by the AIS mode of MARSIS, as a function of $F_{10.7}$ at Mars. Each successive 100 values of N_0 are represented by one cross whose position indicates the mean values of N_0 and $F_{10.7}$. The horizontal bar of each cross, where visible, indicates the range in $F_{10.7}$ at Mars experienced during the 100 measurements. The vertical bar of each cross, where visible, indicates the error in the mean value of N_0. Colours indicate the dates of the measurements. Blue, red, and turquoise data points were acquired between 14 August 2005 and 31 January 2006, 31 January 2006 and 16 February 2007, and 16 February 2007 and 1 August 2007, respectively. The black solid line is the best fit of the data to a function of the form $N_0 \propto F_{10.7}^k$. The best-fit value of k is 0.30 ± 0.04 and the correlation coefficient for the fit is 0.88. Reproduced from Fig. 8 of Morgan et al. (2008). Copyright 2008 American Geophysical Union. Reproduced by permission of American Geophysical Union. (For interpretation of colour mentioned in this figure caption the reader is referred to the web version of the article.)

a proxy, the $F_{10.7}$ index, is often used to represent F in Eq. (8). This proxy is measured at Earth, so it should be corrected for the different (and variable) radial distance of Mars. It should also be corrected because the Sun's EUV irradiance is not uniform across the solar surface. Variations in solar irradiance due to the rotation of active regions around the Sun can be corrected for by shifting the $F_{10.7}$ index in time by an amount equal to the solar rotation period × the Earth–Sun–Mars angle/360° (e.g., Withers and Mendillo, 2005). True temporal variations in the irradiance emitted by localized regions, such as solar flares, are more difficult to correct for (Woods et al., 2006).

The precise relationship between observed peak electron density and $F_{10.7}$ is not clear. It has often been assumed that $N_0 \propto F_{10.7}^k$, where k is an exponent, but attempts to fit data to this expression have found a wide range of exponents. Hantsch and Bauer (1990), Breus et al. (2004), Withers and Mendillo (2005), Zou et al. (2006) and Morgan et al. (2008) found exponents of 0.36, 0.37 ± 0.06, 0.243 ± 0.031, 0.44 and 0.30 ± 0.04, respectively. With the exception of Morgan et al. (2008), who used MARSIS AIS mode data, all these publications used radio occultation data. Fig. 15 shows the fit of data to this expression performed by Morgan et al. (2008). Assuming that H and α are independent of solar irradiance, Chapman theory predicts $N_0 \propto F_{10.7}^{0.5}$ — if $F_{10.7}$ is proportional to F (Eq. (8)). Plausible reasons for the large differences between the observed exponents and 0.5 include the possibility that $F_{10.7}$ is not proportional to F and inadequate characterization of possible variations of H and α with $F_{10.7}$ (Eq. (8)). Until the dependences of H and α on solar irradiance are fully characterized, and their dependences on additional factors like neutral atmospheric conditions are accounted for, it seems unlikely that an expression of the form $N_0 \propto F_{10.7}^k$ will be found that is accurate under all conditions.

Nielsen et al. (2006) used subsets of MARSIS AIS data to study variation in the subsolar peak electron density, N_0, with time. Between July and October 2005, they found that N_0 varied sinusoidally between $1.6 \times 10^5\ \mathrm{cm}^{-3}$ and $2.0 \times 10^5\ \mathrm{cm}^{-3}$ over a period of approximately 26 days, as shown in Fig. 16, consistent with the solar rotation period. The solar rotation affects N_0 because F is affected by the solar rotation. The total EUV irradiance of the face of the Sun that is visible from Mars varies with time as spatial inhomogeneities, or active regions, on the solar disk rotate in and out of view. Several other groups have discerned the effects of solar rotation on radio occultation measurements of peak electron density (Breus et al., 2004; Withers and Mendillo, 2005).

True temporal variations in solar output also affect F. The MARSIS AIS mode measured peak electron density during an X1.1 solar flare on 15 September 2005. Although solar flares are most commonly thought of as increasing the Sun's X-ray output, they increase solar irradiance at all ionizing wavelengths. Peak electron density during the flare increased by more than 30% then returned to its prior value (Gurnett et al., 2005; Gurnett et al., 2008). This rise and fall in peak electron density occurred in less than 7 min, as shown in Fig. 17. The electron density profiles measured

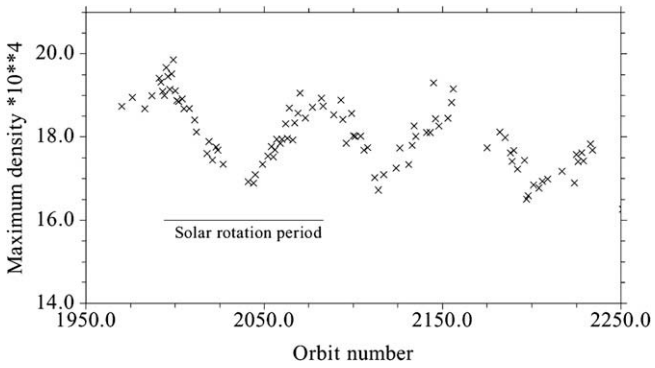

Fig. 16. MARSIS AIS mode measurements of subsolar peak electron density, N_0, in units of cm^{-3} as a function of Mars Express orbit number, which increases linearly with time, from 22 July to 14 October 2005. The horizontal line indicates the duration of one solar rotation period, 26 days. Reproduced from Fig. 3 of Nielsen et al. (2006). With kind permission of Springer Science and Business Media: Fig. 3 of Nielsen et al. (2006).

during this flare will provide unique insight into how the martian ionosphere responds to sudden changes in irradiance. This is the only solar flare whose effects on the martian ionosphere have been reported by MARSIS. It is unfortunate that MARSIS has operated during a prolonged and deep solar minimum characterized by a paucity of solar flares.

Safaeinili et al. (2007) used the MARSIS SS mode to measure ionospheric total electron content and other moments of the electron density profile as function of SZA for $60° < SZA < 100°$. Inferred subsolar electron densities were 50% greater in dawn (or sunrise) data than in dusk (or sunset) data, as shown in Fig. 18. It is highly unlikely that the distribution of solar irradiances sampled by the dawn subset of measurements differed significantly from that sampled by the dusk subset of measurements. In that case, if the ionosphere were a perfect Chapman layer and neutral atmospheric conditions depended only on SZA, not local time, then the dawn and dusk results should be identical. The dawn–dusk difference in inferred

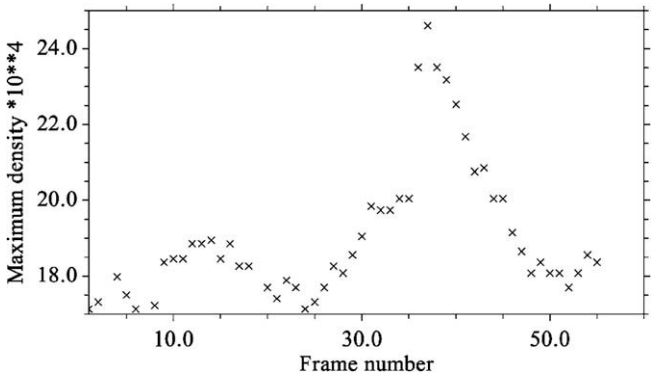

Fig. 17. MARSIS AIS mode measurements of peak electron density, N_m, in units of cm^{-3} during an X1.1 class solar flare on 15 September 2005 as a function of frame number, which increases linearly with time. Seven minutes of data are shown. SZA remained between 30° and 40° during this interval, so changes in N_m due to changes in SZA are negligible. Reproduced from Fig. 4 of Nielsen et al. (2006). With kind permission of Springer Science and Business Media: Fig. 4 of Nielsen et al. (2006).

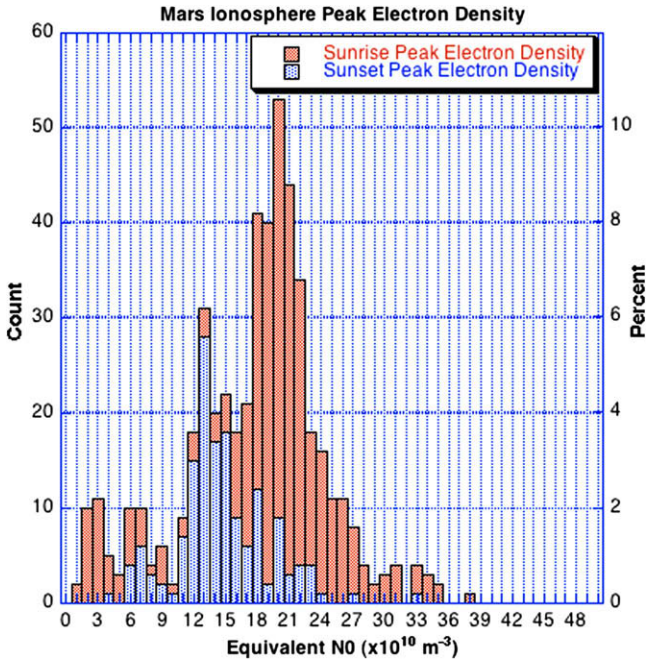

Fig. 18. Histogram of approximately 750 values of subsolar peak electron density, N_0, derived from MARSIS SS mode measurements. Values of N_0 were found from the dependence of N_m on SZA for $60° < SZA < 100°$. Red (blue) columns contain values inferred from measurements made across the sunrise (sunset) terminator. SZA=90° at the terminator. The mean value of N_0 found from the sunrise (sunset) data is 2.1×10^5 cm^{-3} (1.3×10^5 cm^{-3}). Reproduced from Fig. 2 of Safaeinili et al. (2007). Copyright 2007 American Geophysical Union. Reproduced by permission of American Geophysical Union. (For interpretation of colour mentioned in this figure caption the reader is referred to the web version of the article.)

subsolar electron densities might be caused by dawn–dusk differences in either the neutral atmosphere or the transport-controlled region of the topside ionosphere, where time constants are relatively long. Photochemical time constants, which are on the order of minutes at the M2 layer, are too short to produce this effect.

5.4. Peak electron density and magnetic fields

As shown in Fig. 19, Nielsen et al. (2007a) observed that some dayside peak electron densities, N_m, measured by the AIS mode of MARSIS were twice as large as expected. After excluding temporal variations in solar irradiance as a possible cause, they found that these enhanced peak electron densities were associated with strong and vertical crustal magnetic fields, and attributed this to an increase in electron temperature caused by a two-stream plasma instability. High electron temperatures reduce dissociative recombination rates and, for constant production rates, lead to increased electron densities (Eq. (8)). Increases in electron temperature of a factor of seven were inferred. Fig. 5 of Nielsen et al. (2007a) shows a derived electron density profile that corresponds to one of these enhanced peak electron densities. Detailed simulations are needed to explain why the altitudes of the enhanced peak electron densities are 20 km lower than usual, and why enhance-

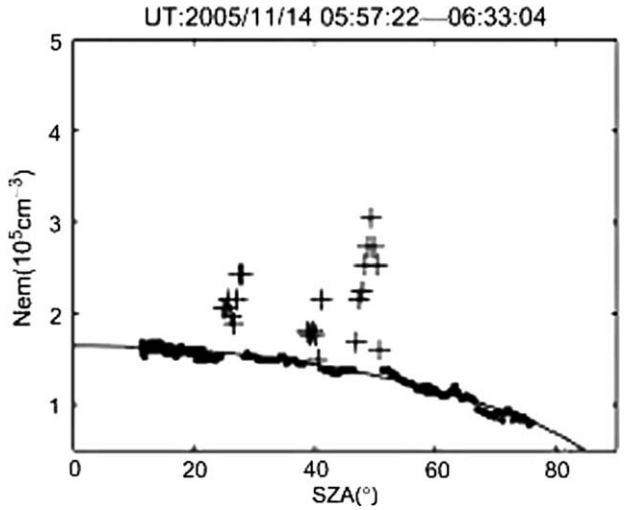

Fig. 19. Peak electron densities, N_m, measured by the MARSIS AIS mode as a function of SZA over a span of approximately 36 min on 14 November 2005. Dots indicate values of N_m that are close to their expected, or "normal", values, whereas crosses indicate values of N_m that are significantly larger than their expected values. The solid line shows a fit of the "normal" data points to a function of the form $N_m = N_0 \cos^{0.5}(SZA)$ (Eq. (4)). Reproduced from Fig. 1 of Nielsen et al. (2007a). Copyright 2007, with permission from Elsevier.

ments in electron density are restricted to the region within 20 km of the usual altitude of the peak of the M2 layer.

Krymskii et al. (2003) used electron density profiles from MGS radio occultations to find that peak electron densities are higher than expected within mini-magnetospheres. Mini-magnetospheres are defined as regions where both ends of magnetic fieldlines that thread the ionosphere intersect with the ground, rather than being open to space. Krymskii et al. (2003) attributed the enhanced peak electron densities to high electron temperatures, and attributed the high electron temperatures to the trapping of hot photoelectrons within the mini-magnetosphere.

High electron temperatures have been found within mini-magnetospheres (Krymskii et al., 2003) and in the cusps at the boundaries of mini-magnetospheres (Nielsen et al., 2007a). However, inferring the direction and topology of the magnetic field on the dayside of Mars at and below the altitude of the M2 layer is not trivial. I use "direction" to refer to the inclination and azimuth of the magnetic field in a localized region and "topology" to refer to the arrangement of magnetic fieldlines with respect to large-scale features like the planetary surface and solar wind. Analyses of electron pitch angle distributions measured by the MGS Electron Reflectometer have determined whether the magnetic fieldline at the location of the spacecraft, typically 400 km altitude, at the time of the measurement is closed, open, draped in the atmosphere/ionosphere, or draped above the atmosphere/ionosphere (Brain et al., 2007). MGS Electron Reflectometer data have also been used to determine the magnetic field magnitude at 185 km altitude (Lillis et al., 2008). Most analyses of the ionospheric effects of magnetic fields infer direction and topology from a model of the crustal magnetic field. Several such models have been produced from nightside MGS vector magnetometer data (Cain et al., 2003; Arkani-Hamed, 2004; Langlais et al., 2004). Although MGS descended below 200 km routinely during its aerobraking and science phasing orbits before settling into its 400 km science orbit, magnetometer data at ionospheric altitudes is relatively sparse. The dayside magnetic field at Mars results from the combination of the piled-up solar wind magnetic field, for which a proxy exists over the duration of the MGS mission (Brain et al., 2003; Crider et al., 2003), and the approximately known, steady crustal magnetic field. However, the dayside magnetic field is not a simple vector sum of these two contributions, since ionospheric currents (which themselves depend on magnetic field direction) produce magnetic fields which can further alter the magnetic field structure. Potential uncertainties in both local magnetic field direction and larger-scale magnetic field topology should be considered when ionospheric phenomena are attributed to magnetic processes.

5.5. Peak altitude and SZA

Peak altitude, z_m, varies with SZA. Eq. (5) predicts that $z_m = z_0 + H \ln Ch$. Several data analysis efforts have concluded that the observed variations are approximately consistent with this prediction, as shown in Figs. 13 and 20. Hantsch and Bauer (1990) used pre-MGS radio occultation data to find that z_0 and H equal 120 km and 10 km, respectively, whereas Morgan et al. (2008) used MARSIS AIS mode data to find that z_0 and H equal 133.6 ± 0.1 km and 8.9 ± 0.2 km, respectively. These scale heights are consistent with independent scale height measurements (Nier and McElroy, 1977; Withers, 2006). The inferred subsolar peak altitude, z_0, can be used to test Eq. (6), $\sigma n(z_0) H = 1$. A scale height of 8.9–10 km and $\sigma = 3 \times 10^{-17}$ cm^2, appropriate for wavelengths of 20–90 nm (Schunk and Nagy, 2000), suggests that n at z_0 is $(3-4) \times 10^{10}$ cm^{-3}. The Viking neutral mass spectrometers measured $n \approx 1 \times 10^{11}$ cm^{-3} at 120 km and $n \approx 3 \times 10^{10}$ cm^{-3} at 133.6 km (Nier and McElroy, 1977). Given the substantial variability of the neutral upper atmosphere with local solar time, longitude, latitude, season and other factors, the neutral densities inferred from ionospheric peak altitudes are consistent with those found by direct measurement (Withers et al., 2003; Withers, 2006).

5.6. Peak altitude and atmospheric densities

The peak altitude, z_m, varies with longitude at fixed latitude, season, SZA and local solar time, as shown in Fig. 21 (Bougher et al., 2001). Large zonal variations in neutral density at ionospheric altitudes have been observed by aerobraking orbiters, as shown in Fig. 22, and are produced by non-migrating thermal tides (Keating et al., 1998; Forbes et al., 2002; Withers et al., 2003). Density variations affect z_m by modifying the altitude at which the optical thickness is unity (Eq. (6)). The amplitudes and wavenum-

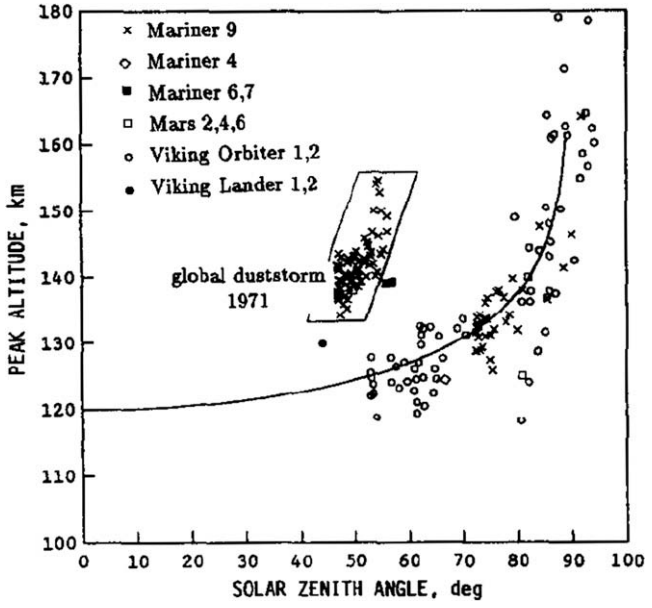

Fig. 20. Altitudes, z_m, of peak electron density as a function of SZA. Data from different missions are indicated by different symbols. With two exceptions, the data points were acquired by radio occultation experiments. The two exceptions are the Viking Lander *in situ* retarding potential analyzer data. The solid line, which is not based on a formal fit to the data points, is given by $z_m = 120\ \text{km} + 10\ \text{km}\ \ln\sec(SZA)$ (Eq. (5)). The solid line provides an adequate representation of many, but not all, of the data points. The most striking discrepancy is that peak altitudes measured by the Mariner 9 radio occultation experiment in 1971, during the waning of a large global dust storm, are 20–30 km higher than expected. Reproduced from Fig. 4 of Hantsch and Bauer (1990). Copyright 1990, with permission from Elsevier.

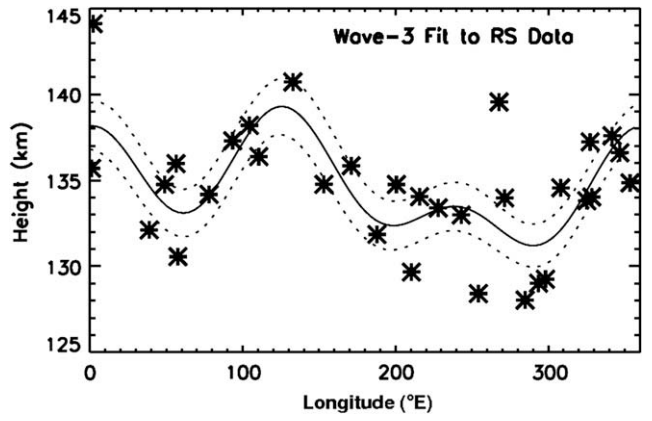

Fig. 21. Height, z_m, of the peak electron density as a function of longitude (asterisks). These 32 data points were acquired by the MGS radio occultation experiment at 64.7°N to 67.3°N, local solar times of 03–04 h, solar zenith angles of 78°–81°, and L_s of 74°–77° in December 1998. The solid line shows the best fit of a wave-3 model to the data points Withers et al. (2003). The dotted lines flanking the solid line are an uncertainty envelope. Reproduced from Fig. 2 of Bougher et al. (2001). Copyright 2001 American Geophysical Union. Reproduced by permission of American Geophysical Union.

bers of the variations in z_m found by the MGS radio occultation experiment are consistent with the zonal variations found in neutral density measurements (Bougher et al., 2001; Bougher et al., 2004).

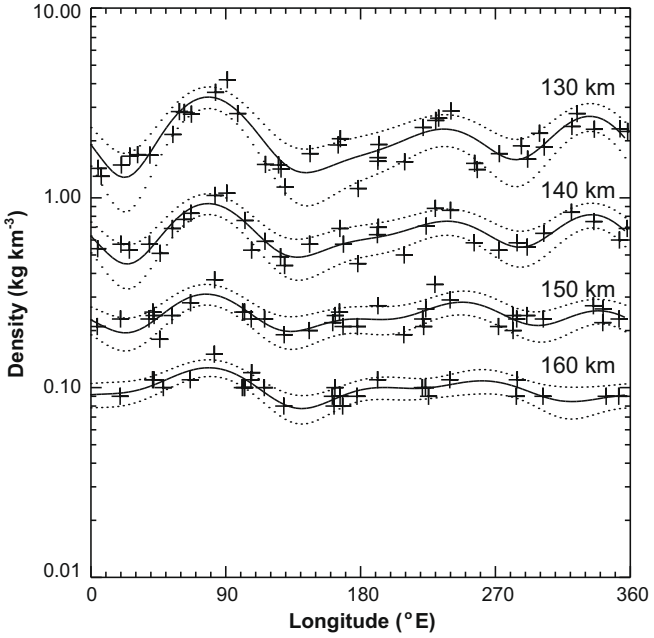

Fig. 22. Outbound density measurements made at various altitudes by the MGS accelerometer (crosses). The data points were measured at 10°N–20°N, mid-afternoon local solar times, and $L_s \approx 90°$. Each solid line shows the best fit of a wave-4 model to the data points and the dotted lines flanking each solid line indicate 1σ uncertainties on the fit. Previously published as Fig. 4 of Withers et al. (2003). Copyright 2003, with permission from Elsevier.

Thermal tides are not the only atmospheric process that affect z_m. Hantsch and Bauer (1990) investigated radio occultation measurements from the Mariner 9 standard mission and found that the M2 layer was 20–30 km higher than usual when an intense global dust storm was subsiding (Fig. 20). Large amounts of dust suspended in the lower atmosphere affect how energy is transported vertically, especially by radiative transfer, and heat the lower atmosphere. The subsequent thermal expansion of the lower atmosphere lifts pressure levels in the upper atmosphere, thereby raising the altitude of the ionospheric peak.

Although the width of the M2 layer is proportional to the scale height of the neutral atmosphere, as discussed in Section 2, variations in this width have not been studied in detail and have only been used in preliminary investigations of the neutral atmosphere (e.g., Morgan et al., 2008).

6. Variability below the M2 layer

The ionospheric region below the M2 layer is more complex than that around the M2 layer, although it is also photochemically controlled. The M1 layer lies below the M2 layer and an additional layer, the meteoric layer, is occasionally observed at 90 km, below the M1 layer. There is indirect evidence for the production of plasma somewhere below the M2 layer by sporadic solar energetic particle events, and theorists have also predicted that cosmic rays should maintain a plasma reservoir at altitudes as low as 35 km.

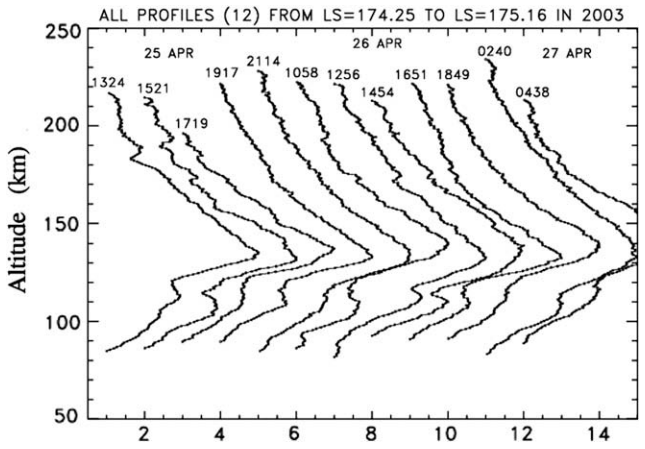

Fig. 23. Twelve electron density profiles obtained by the MGS radio occultation experiment on 25–27 April 2003. Four digit numbers above each profile indicate UTC time. For the first profile, the horizontal axis is the logarithm (base 10) of electron density in cm^{-3}. Peak electron density in the first profile is thus 10^5 cm^{-3}. The horizontal axis for the second profile is the same, except that the second profile is shifted to the right by one unit with respect to the preceding profile. This shift is repeated for all profiles and is intended to provide visual clarity for the reader. All profiles were acquired at the same latitude (74°N), SZA (74°), and local solar time (13:45). The shape, altitude and electron density of the M1 layer vary greatly within this small set of observations. Previously published as Fig. 4 of Christou et al. (2007). Reproduced by permission of Claude Bertaut, Editor-in-Chief of Astronomy and Astrophysics.

6.1. M1 layer properties and time

Fig. 23 shows 12 electron density profiles obtained by the MGS radio occultation experiment on 25–27 April 2003 (Christou et al., 2007). All profiles were acquired at the same latitude, SZA and local solar time. The shape, altitude and electron density of the M1 layer vary greatly within this small set of observations. The interval between successive profiles is a few hours. Determination of the shape, altitude and electron density of the M1 layer is very difficult when the layer is not associated with a local maximum in electron density, but is instead merely a shoulder below the M2 layer. Even when a local maximum is present, it is often small in comparison to the measurement uncertainties, which makes it challenging to quantify the M1 layer's shape, altitude and electron density with uncertainties that are small enough to make the results useful. Automated measurement of properties of the M1 layer has proven so difficult that several groups have been forced to use irreproducible manual methods instead.

6.2. M1 layer and Chapman theory

Chapman theory has not been applied to radio occultation observations of the M1 layer as successfully as it has been applied to observations of the M2 layer (Bougher et al., 2001; Fox and Yeager, 2006). The monochromatic assumption of Chapman theory fails at the M1 layer because, for the wavelengths shorter than 20 nm that produce the M1 layer, the ionization cross-section of CO_2 decreases significantly as wavelength decreases (Fig. 2). The ionization cross-section of CO_2 is effectively constant for the 20–90 nm photons responsible for the M2 layer, so the assumptions that underpin Chapman theory are valid at the M2 layer. The importance of electron impact ionization, which causes the number of ion–electron pairs produced per photon absorbed to vary strongly with wavelength at wavelengths shorter than 20 nm, at the M1 layer also reduces the applicability of Chapman theory. More sophisticated photochemical models are necessary for analysis of the M1 layer, but even the best current models fail to reproduce the M1 layer well (Fox, 2004b).

Fig. 24 shows two electron density profiles simulated by Bougher et al. (2001). One was generated with a standard solar spectrum, the other was generated using a modified solar spectrum in which the irradiance at all wavelengths shorter than 15 nm was increased by an order of magnitude. Above the peak of the M2 layer, electron densities are slightly increased, but the profile's shape is not altered. Below the peak of the M2 layer, electron densities are increased significantly and the shape of the profile is drastically altered. Electron densities are increased at all altitudes when short wavelength solar irradiance is increased. A faint shoulder at 100 km in the "standard" profile becomes a clear M1 layer in the "enhanced" profile. Electron densities at the altitude of the M1 layer change by the square root of 10, as expected for molecular ions lost by dissociative recombination (Rishbeth and Garriott, 1969; Bougher et al., 2001). Fox (2004b) used a model to predict that electron densities at the altitude of the M1 layer change by the square root of the factor by which the solar irradiance shortward of 20 nm increases. Inadequate knowledge of solar irradiance at the appropriate spectral and temporal resolutions makes it challenging to model specific observations of the M1 layer.

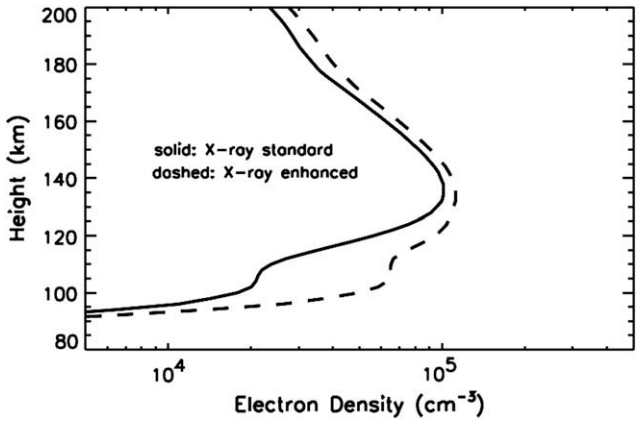

Fig. 24. Two electron density profiles simulated by Bougher et al. (2001). The solid line indicates a profile generated using a standard solar spectrum and the dashed line indicates a profile generated using a modified solar spectrum in which the irradiance at all wavelengths shorter than 15 nm was increased by an order of magnitude. Conditions are as in Fig. 21. Reproduced from Fig. 4 of Bougher et al. (2001). Copyright 2001 American Geophysical Union. Reproduced by permission of American Geophysical Union.

6.3. Peak electron density in the M1 layer and SZA

The peak electron density in the M1 layer varies with SZA. Fox and Yeager (2006) assumed that peak electron density is proportional to $\cos^k$(SZA), then determined values of k, the exponent, equal to 0.55 for low solar activity, 0.551 ± 0.024 for moderate solar activity, and 0.53 for high solar activity from a study of radio occultation measurements. These values are close to the exponent of 0.5 expected for a photochemically controlled ionospheric region where the dominant ion loss process is the dissociative recombination of molecular ions, as discussed in Section 2, even though the M1 layer is not described well by Chapman theory.

6.4. Unusually small electron densities in the M1 layer

Fig. 25 shows four examples of MGS radio occultation electron density profiles that have unusually small electron densities in the M1 layer (Withers et al., 2006). These unusual profiles could be indicative of low ion production rates or high ion loss rates, but their cause has not been investigated. Possibilities include temporal variations in either solar irradiance or the neutral atmosphere and spatial variations in the neutral atmosphere.

6.5. Electron densities in and below the M1 layer during solar flares

The high cadence MARSIS AIS observations during a solar flare cannot measure electron densities in the M1 layer. In certain fortuitous cases, low cadence radio occultation experiments have measured electron density profiles affected by solar flares. Fig. 26 shows MGS radio occultation electron density profiles acquired within minutes of a solar flare on 15 April 2001 (X14.4 class flare) and 26 April 2001 (M7.8 class flare) (Mendillo et al., 2006). Electron densities above the M2 layer did not change by more than the measurement uncertainties, yet electron densities at lower altitudes were significantly increased. The relative change in electron density increased as altitude decreased, which is consistent with hardening of the solar spectrum

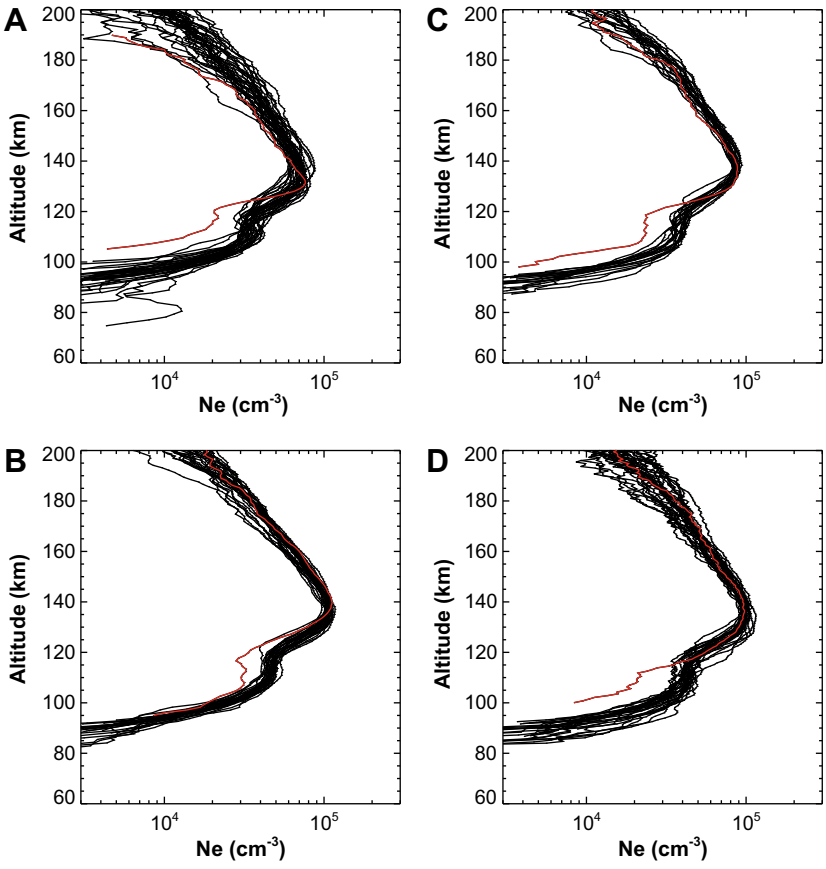

Fig. 25. Four panels of MGS radio occultation electron density profiles. (A) Profile 0351C17B.EDS (red line) was measured at latitude 68.6°N, longitude 90.5°E, 2.8 h LST, $L_s = 89.9°$ and SZA = 81.3° on 16 December 2000 (UTC). The black lines show 33 profiles measured under similar conditions on 15–17 December. (B) Profile 1120B42A.EDS (red line) was measured at latitude 81.9°N, longitude 40.2°E, 8.7 h LST, $L_s = 153.6°$ and SZA = 74.1° on 30 April 2001 (UTC). The black lines show 27 profiles measured under similar conditions on 29 April–1 May. (C) Profile 1138L20A.EDS (red line) was measured at latitude 77.9°N, longitude 56.3°E, 7.6 h LST, $L_s = 163.3°$ and SZA = 78.3° on 18 May 2001 (UTC). The black lines show 19 profiles measured under similar conditions on 17–19 May. (D) Profile 3114L58A.EDS (red line) was measured at latitude 74.3°N, longitude 98.9°E, 13.7 h LST, $L_s = 173.7°$ and SZA = 73.4° on 24 April 2003 (UTC). The black lines show 27 profiles measured under similar conditions on 23–25 April. (For interpretation of colour mentioned in this figure caption the reader is referred to the web version of the article.)

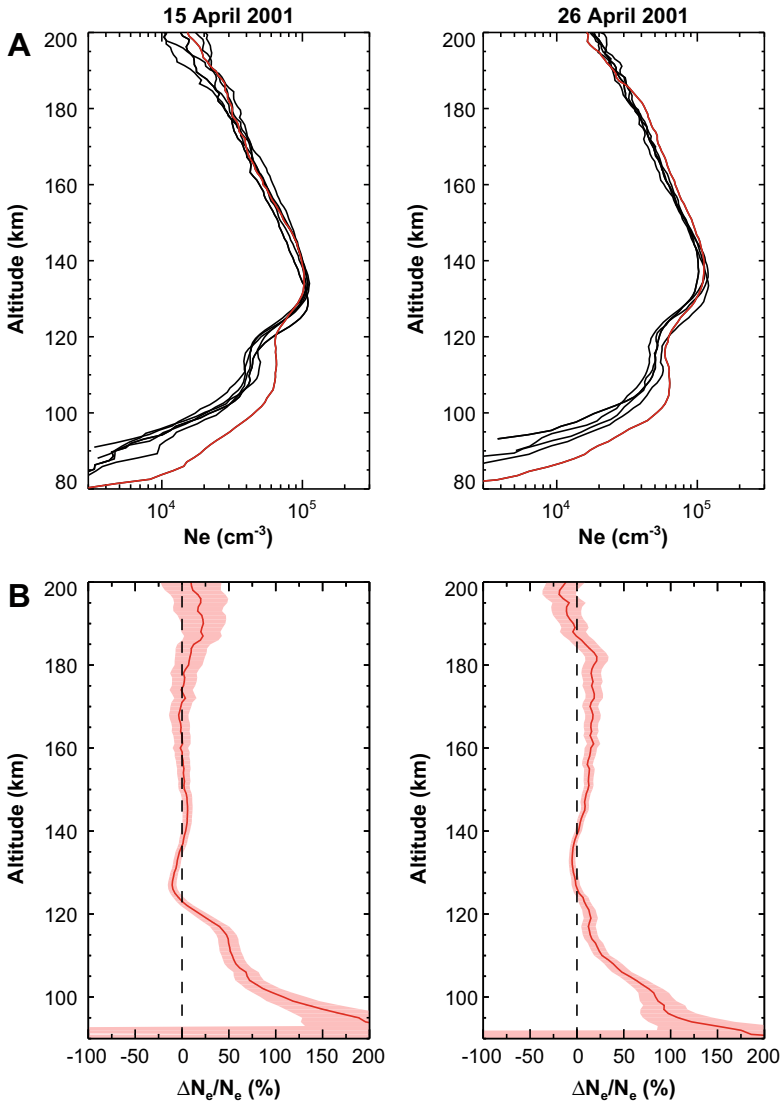

Fig. 26. (A) MGS radio occultation electron density (Ne) profiles on Mars obtained for 15 April and 26 April 2001. Measurement uncertainty is several thousand electrons per cm^3, and thus the two profiles in red (14:15 and 13:16 UTC, respectively) show statistically significant departures at low altitudes because of solar flares. On 15 April, there were five MGS profiles before the flare, at 02:28, 06:23, 08:21, 10:19, and 12:17 UTC, and none after the flare; on 26 April, preflare profiles were available at 09:20 and 11:18 UTC, and postflare profiles were available at 17:11 and 19:09 UTC. (B) Percentage differences between the flare-affected profiles and the averages of the other profiles on each day. The shadings give the 1σ standard error in the relative change in electron density. Previously published as Fig. 1 of Mendillo et al. (2006). Reprinted with permission from AAAS.

during a solar flare. Consequently, the shape of the lower ionosphere changes during a solar flare. The increase in electron densities in the M1 layer can be substantial. In these two examples, electron densities at 100 km doubled. The enhancements in electron density in these two examples are similar, despite the differences in peak flare magnitude, because the ionospheric observation associated with the larger flare occurred longer after the flare peak than for the smaller flare (Mendillo et al., 2006).

6.6. The importance of the M1 layer for radio wave propagation

The fate of MARSIS AIS mode transmissions depends on the transmission frequency. At frequencies less than the maximum value of f_p (Eqs. (11) and (12)), the radio transmissions are reflected by the ionosphere and detected at the spacecraft. At frequencies greater than the maximum value of f_p, the radio transmissions penetrate the ionosphere, reflect at the ground, and are detected at the spacecraft. Ground reflection signals are attenuated by twice passing through the ionosphere and their strength can be below the instrument's detection threshold if they experience substantial attenuation. The attenuation is frequency-dependent, which typically causes MARSIS to fail to detect ground reflections at frequencies slightly greater than the maximum value of f_p. Nielsen et al. (2007b) modelled the performance of the MARSIS instrument and the attenuation of radio waves by the ionosphere, and calculated that the ground reflection should disappear if the ionospheric attenuation exceeded 26.0 dB (24.1 dB) for a spacecraft altitude of 293 (358) km. Nielsen et al.

(2007b) then examined the minimum frequency at which ground reflections were detected by MARSIS, as shown in Fig. 27. They found that the observed dependence of this minimum frequency on SZA was consistent with the attenuation predicted by an ionospheric model, which suggests that the model is realistic, if the model included the M1 layer, M2 layer and topside, but not if the model neglected the low altitude M1 layer. This indicates the importance of the M1 layer for radio wave propagation, even though it is a relatively minor contributor to the total electron content of the ionosphere.

6.7. Meteoric layer

Electron density profiles from radio occultation experiments sometimes contain detectable plasma below the M1 layer. Figs. 28 and 29 show that an additional layer of plasma is sometimes present at 80–100 km (Pätzold et al., 2005; Withers et al., 2008). It has been identified in 71 of 5600 and 75 of 465 MGS and Mars Express radio occultation electron density profiles, respectively (Withers et al., under review). In MGS radio occultation observations, the mean altitude of the meteoric layer is 91.7 ± 4.8 km, the mean peak electron density in the meteoric layer is $(1.33 \pm 0.25) \times 10^{10}$ m^{-3}, and the mean width of the meteoric layer is 10.3 ± 5.2 km. Meteoric layer altitude, peak electron density and width are all positively correlated, with correlation coefficients of 0.3–0.4. Other correlation coefficients between the physical characteristics of meteoric layers and atmospheric or observational properties, such as solar irradiance, neutral scale height and SZA, have absolute values that are significantly smaller, indicating lack of correlation. This is in stark contrast with the behaviour of the photochemically controlled M2 layer,

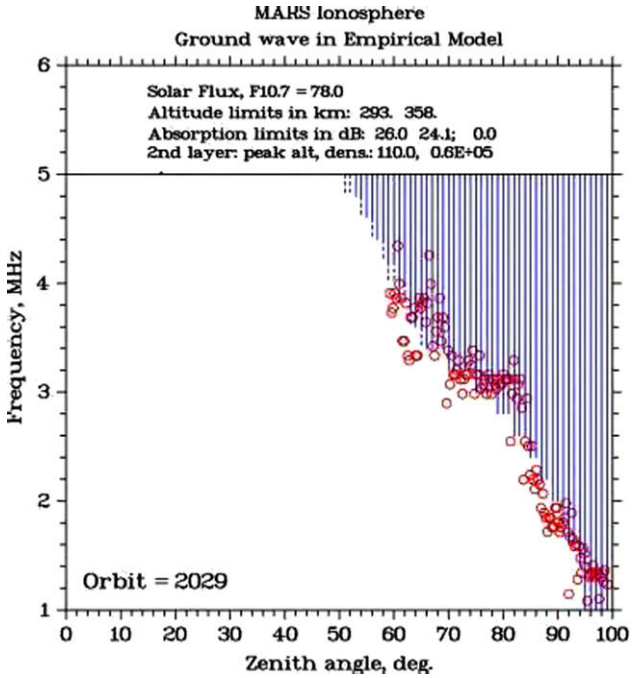

Fig. 27. Minimum frequency at which ground reflections were detected in measurements by the MARSIS AIS mode on orbit 2029 as a function of SZA (open red circles). The lowest points on the solid (dashed) vertical blue lines indicate the predicted minimum frequency, assuming that ground reflection is lost when ionospheric attenuation exceeds 26.0 (24.1) dB. A range of threshold attenuation values is considered in order to account for variations in spacecraft altitude during the observations. Reproduced from Fig. 9 of Nielsen et al. (2007b). Copyright 2007, with permission from Elsevier.

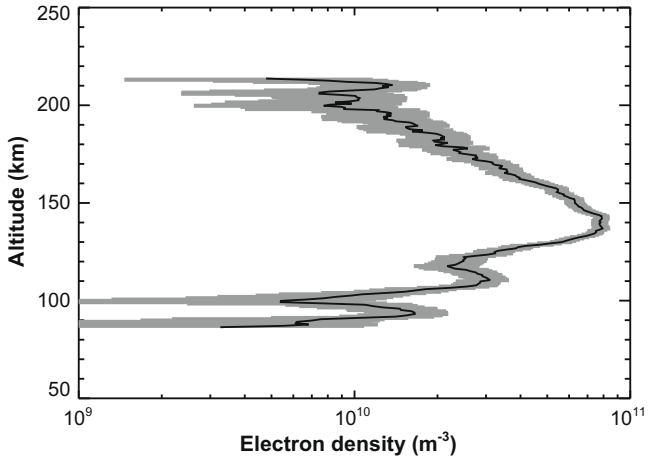

Fig. 28. MGS radio occultation profile 5045K56A.EDS has three clear layers, the M2 layer at 140 km, the M1 layer at 110 km and the meteoric layer at 90 km. It was measured at latitude 79.9°N, longitude 316.0°E, 9.9 h LST, $L_s = 160.1°$ and SZA = 73.2° on 14 February 2005. Lines and shading as Fig. 4. Previously published as Fig. 2 of Withers et al. (2008). Copyright 2008 American Geophysical Union. Reproduced by permission of American Geophysical Union.

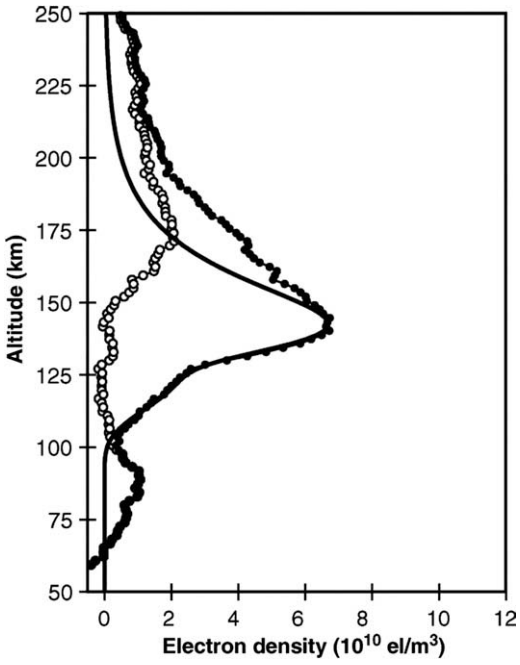

Fig. 29. Electron density profile (solid disks) measured by the Mars Express radio occultation experiment on 18 April 2004, orbit 314. The M2 layer is present at 150 km, the M1 layer is visible as a shoulder at 120 km, and the meteoric layer is present at 85 km. The solid line is a fit of two Chapman functions to the M2 and M1 layers. The open circles show the difference between the data and the fit. Reproduced from Fig. 1 of Pätzold et al. (2005). Reprinted with permission from AAAS.

whose properties do depend on solar irradiance, neutral scale height and SZA. The occurrence rate of the meteoric layer varies strongly with season, often varying by an order of magnitude, which is consistent with control of this meteoric layer by variations in meteoroid flux (Withers et al., under review).

6.8. Production of low-altitude plasma during energetic particle events

The MARSIS AIS mode usually detects ground reflections at high frequencies. However, all ground reflections are sometimes absent for periods of about one week, as shown in Fig. 30 (Morgan et al., 2006; Morgan et al., in press). Similar absences were found by the MARSIS SS mode (Espley et al., 2007). Morgan et al. (2006) found that the MARSIS AIS mode failed to detect ground reflections when Mars was bombarded by large fluxes of energetic particles associated with coronal mass ejections. Morgan et al. (in press) found that the passage of a corotating interaction region by Mars also prevented the detection of ground reflections by the MARSIS AIS mode. Espley et al. (2007) similarly concluded that the MARSIS SS mode failed to detect ground reflections when Mars was bombarded by solar energetic particles. The absence of ground reflections implies that plasma at some point along the ray path is able to absorb the electromagnetic radiation. The absence of ground reflections during the bombardment of Mars by energetic particles has been attributed to the production of plasma by these energetic particles. The amount of plasma produced by energetic particles, its vertical distribution, and its lifetime have not yet been derived from the MARSIS measurements (Morgan et al., 2006; Nielsen et al., 2007b) nor predicted theoretically (Molina-Cuberos et al., 2001; Molina-Cuberos et al., 2002; Leblanc et al., 2002). Simulations of MARSIS attenuation during normal conditions, such as those performed by Nielsen et al. (2007b), have not been extended to include the response to an energetic particle event. This is because existing studies of the martian response to energetic particle events have not reported predictions for how electron densities in the martian ionosphere vary with altitude and time (Molina-Cuberos et al., 2001; Molina-Cuberos et al., 2002; Leblanc et al., 2002). Such predictions, coupled with simulations of MARSIS attenuation, would enable quantitative comparisons of attenuation observations to predictions, which would test whether the models are realistic or not. At present, the association between the absence of ground reflections and energetic particle events has only been demonstrated qualitatively. All that has been concluded at this point is that the excess plasma is below the M2 layer, the termination point of MARSIS electron density profiles. Examination of low-altitude plasma densities in radio occultation profiles obtained by MGS or Mars Express during these energetic particle events, if such profiles exist, might be fruitful.

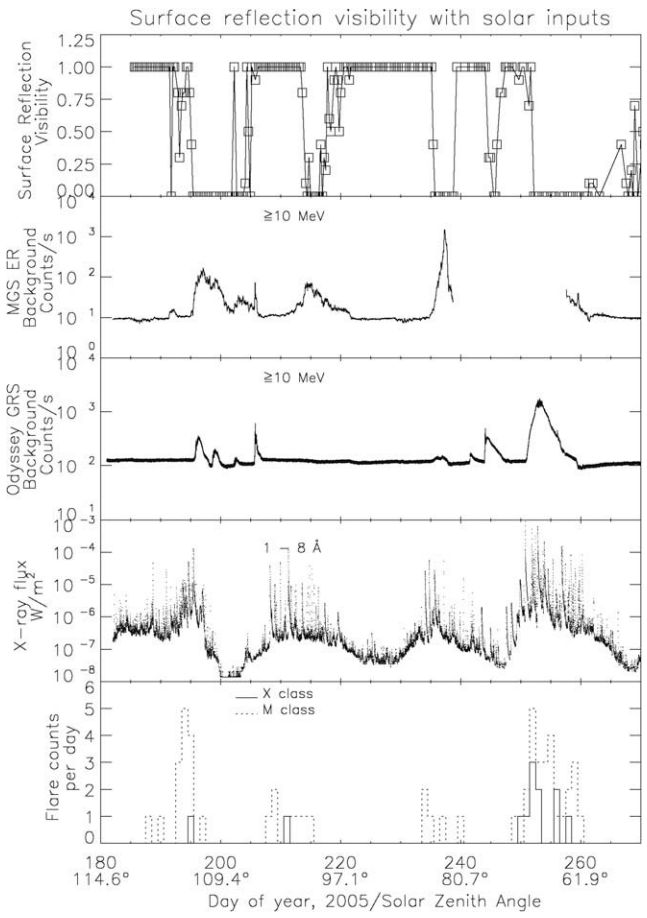

Fig. 30. The ability of the AIS mode of the MARSIS instrument to detect ground reflections depends on solar energetic particle events. "A time series plot comparing surface reflection visibility averaged over 10 samples nearest 850 km altitude on the outbound leg of an orbit, with orbital period of 7.5 h (first panel). [The surface reflection visibility for a MARSIS ionogram is defined as 1 if the ground reflection is visible and 0 if it is not.] Also shown are Mars Global Surveyor Electron Reflectometer background (second panel), Mars Odyssey Gamma Ray Spectrometer (Upper Level Discriminator) background (third panel), soft X-ray emissions measured by the Solar Environment Monitor aboard GOES 12, with time adjusted for propagation to Mars (fourth panel), and NOAA daily flare counts (fifth panel). The abscissa of all plots is decimal day of year, 2005, accompanied by the solar zenith angle of the spacecraft where the samples shown in Fig. 1 were taken" Morgan et al. (2006). Reproduced from Fig. 2 of Morgan et al. (2006). Copyright 2006 American Geophysical Union. Reproduced by permission of American Geophysical Union.

6.9. Production of low-altitude plasma by cosmic rays

As shown in Fig. 31, models have predicted that cosmic rays produce a permanent reservoir of low altitude plasma with electron densities in excess of 100 cm^{-3} at 35 km (Molina-Cuberos et al., 2001; Molina-Cuberos et al., 2002). Low altitude plasma strongly attenuates radio signals, so the attenuation of MARSIS transmissions can be used to measure or place upper limits on electron densities at very low altitudes, thereby testing these predictions. MARSIS-derived upper limits on electron densities in the lower atmosphere have not yet been reported.

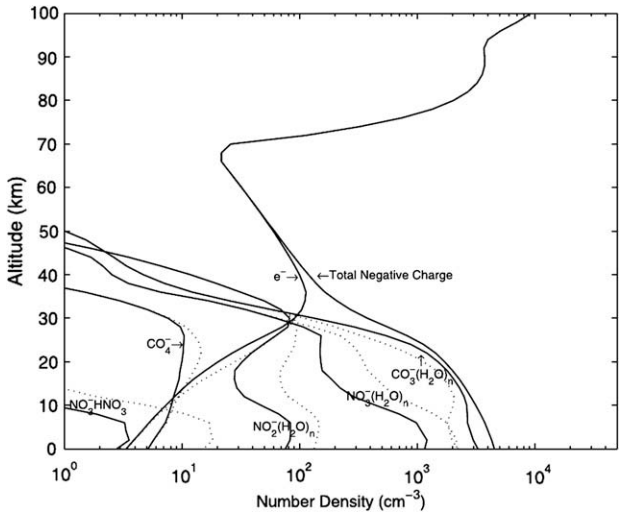

Fig. 31. Predicted electron densities and anion concentrations in the lower martian ionosphere. Solid (dotted) lines correspond to a high (low) water abundance of 8.8 (3.0) precipitable microns. Reproduced from Fig. 6 of Molina-Cuberos et al. (2001). Copyright 2001, with permission from Elsevier.

7. Variability above the M2 layer

The ionospheric region above the M2 layer is more complex than that around the M2 layer. It contains a mixture of atomic and molecular ions, and it is affected by both photochemical and transport processes. The significance of transport processes above the M2 layer, and its proximity to the solar wind and the upper boundary of the ionosphere, mean that magnetic field strength, direction and topology are potentially important here.

7.1. Changes in topside scale height with altitude

Viking-era radio occultation electron density profiles (Zhang et al., 1990b; Kliore, 1992) and the Viking 1 RPA profile (Fig. 3) do not show a change in scale height in the topside ionosphere, but the Viking 2 RPA profile does (Fig. 3, around 180 km). A similar change in scale height is common in MARSIS profiles (Fig. 6, around 210 km) and Mars Express radio occultation profiles (Fig. 32, around 230 km). This change in scale height is not common in MGS radio occultation profiles (Fig. 4), which may be because they do not extend as high as those of other radio occultation experiments due to the low orbit of MGS.

There is a transition in most ionospheres from a photochemically controlled region at low altitudes to a transport-controlled region at high altitudes (Rishbeth and Garriott, 1969). Theory suggests this occurs around 200 km on Mars (Nagy and Cravens, 2002). A change in scale height is common at an ionosphere's photochemical/transport boundary because plasma in the topside of a Chapman layer has a scale height of twice the neutral scale height, whereas plasma in diffusive equilibrium in a transport-controlled region has a scale height that is proportional to the sum

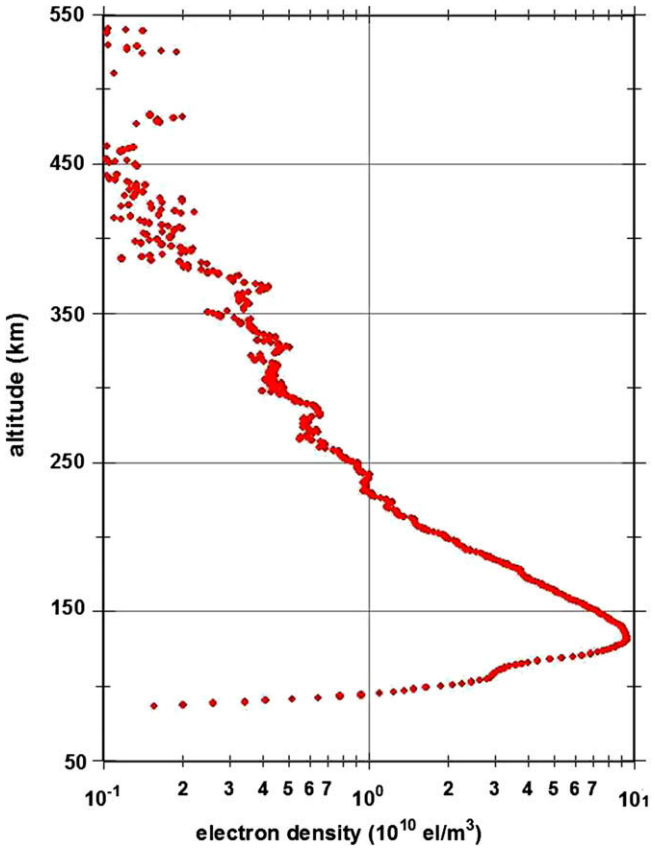

Fig. 32. A typical Mars Express radio occultation electron density profile that shows a change in the topside scale height at about 230 km altitude. These data were acquired at latitude 61.1°N, longitude 211.4°E, 13.4 h LST, $L_s = 349.2°$ and SZA = 67.7° on 31 December 2005 (orbit 2528).

of the ion and electron temperatures and inversely proportional to the ion mass (Rishbeth and Garriott, 1969). The change in scale height found in several types of observations in the vicinity of 200 km altitude is likely to correspond to the photochemical/transport boundary.

The absence of an increase in plasma scale height above the photochemical/transport boundary in most Viking-era observations was interpreted to mean that plasma scale heights are significantly smaller than diffusive equilibrium would predict given the ion and electron temperatures measured by the Viking Lander RPA instrument (Nier and McElroy, 1977; Hanson et al., 1977; Hanson and Mantas, 1988). These small plasma scale heights were then interpreted as evidence for the presence of horizontal magnetic fields that impede vertical motion of plasma (Section 2) (Hanson and Mantas, 1988; Shinagawa and Cravens, 1989; Shinagawa and Cravens, 1992).

7.2. Abrupt changes in topside electron density with altitude above strong magnetic fields

Fig. 33 shows six MGS radio occultation electron density profiles that contain unusually large changes in electron density over short vertical distances (Withers et al., 2005). There are some cases of localized decreases in elec-

tron density and some cases of localized increases in electron density. Such profiles were classified as "anomalous". Of the MGS radio occultation profiles available to Withers et al. (2005), only 5 of 3529 profiles from the northern hemisphere were anomalous, whereas 20 of 220 profiles from the southern hemisphere were anomalous. The 20 anomalous profiles from the southern hemisphere are located over regions of strong crustal magnetic fields, and regions of strong crustal fields occupy a much smaller fraction of the northern hemisphere. Withers et al. (2005) concluded that the presence of strong magnetic fields is a necessary condition for the production of anomalous profiles. The true nature of these anomalous features is not yet clear. In particular, it is not known whether the occurrence of anomalous features in some, but not all, profiles above strong crustal fields results from anomalous features only occurring in certain magnetic field structures, anomalous features only occurring under certain solar wind conditions, or some other reason. It is also uncertain whether an anomalous feature would be present in a repeated observation at the same latitude, longitude, season, local time, and SZA.

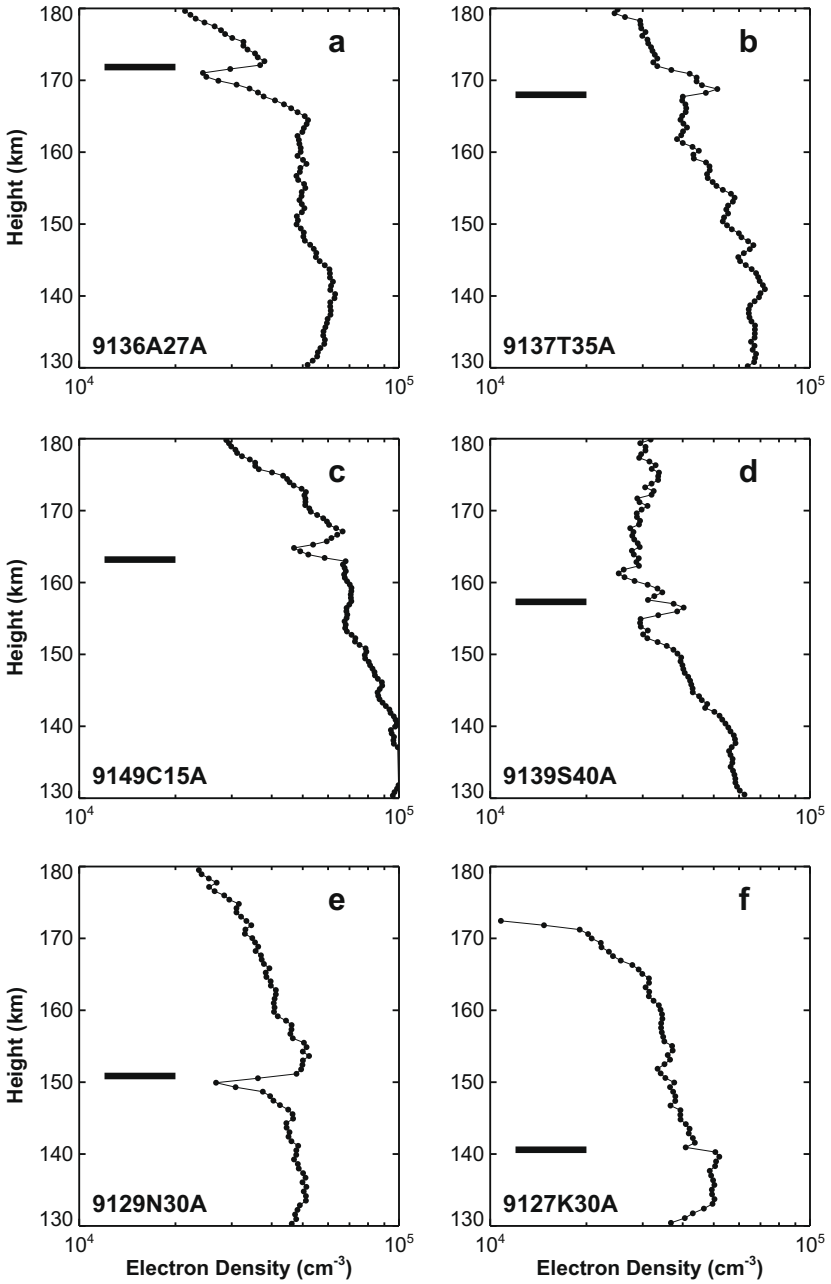

Fig. 33. Six anomalous MGS radio occultation electron density profiles. The profiles are marked by solid circles, linked by a thin solid line, at each data point. The height of each anomalous feature is marked by a thick horizontal bar. Profile names are also given (e.g., 9136A27A). Previously published as Fig. 2 of Withers et al. (2005). Copyright 2005 American Geophysical Union. Reproduced by permission of American Geophysical Union.

7.3. Enhanced topside electron densities above strong and vertical magnetic fields

A typical MARSIS AIS mode ionogram (Fig. 5) contains one ionospheric echo from directly below the spacecraft. Some ionograms, such as Fig. 34, contain multiple echoes. The first of these echoes is the nadir reflection, the second comes from a more distant source. Duru et al. (2006) found that the sources of these off-nadir reflections are fixed and localized, as shown in Fig. 35. They interpreted the cause of these unusual echoes to be regions of enhanced electron density and determined that electron density enhancements "coincide with regions where the crustal magnetic field is strong and nearly vertical". Similar results were found by Nielsen et al. (2007c). Duru et al. (2006) found that the apparent altitudes of the vertices of many of their hyperbolic traces were higher than the usual apparent altitude of the corresponding nadir reflection, which suggests that MARSIS passed directly above the structure responsible for the hyperbolic trace. The enhancements reported by Duru et al. (2006) are substantial. The apparent range from the spacecraft to electron densities of $4.5 \times 10^4\ \mathrm{cm}^{-3}$ ($f_p = 1.9$ MHz) is about 20 km less than expected, on average, over these regions. Assuming that the change in true range is also 20 km, and that the topside ionosphere at this plasma density is Chapman-like and therefore has a plasma scale height of twice the neutral scale height, this corresponds to an increase in electron density at fixed altitude by a factor of 2.7. Ness et al. (2000) also found suggestions of enhanced electron densities in Mariner 9 radio occultation data above strong and vertical crustal fields. In addition, Mitchell et al. (2001) used MGS Electron Reflectometer data to conclude that the ionosphere's extent is greatest above strong crustal fields, but did not consider whether the field's direction influenced this.

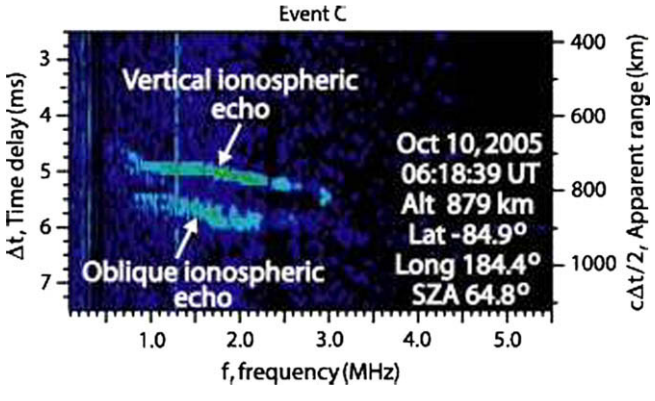

Fig. 34. This MARSIS AIS mode ionogram contains two traces. The upper trace indicates the reflection of radio waves from the ionosphere directly below the spacecraft. The lower trace, whose apparent range exceeds the spacecraft altitude, cannot come from the nadir direction. It must be an oblique echo from a more distant reflector. A colour scale is not present in the original image. Reproduced from Fig. 8 of Gurnett et al. (2008). Copyright 2008, with permission from Elsevier.

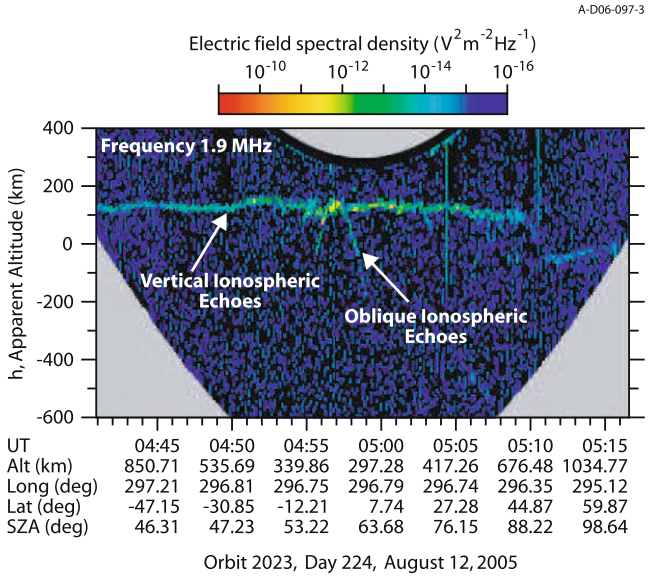

Fig. 35. A radargram (not ionogram) obtained by the AIS mode of the MARSIS instrument that contains an oblique echo. The vertical axis is apparent altitude, defined as spacecraft altitude minus apparent range, and the horizontal axis is time. Colours indicate the strength of the reflected radio signal at a single frequency, 1.9 MHz. Vertical reflection from the ionosphere beneath the spacecraft causes the horizontal trace at an apparent altitude of ≈130 km. An off-nadir reflection from a more distant source causes the hyperbolic trace centred on a time of 04:57. The negative apparent altitudes confirm that the source is not directly below the spacecraft. The shape of this trace indicates that the source of the off-nadir reflection is fixed and localized. Reproduced from Fig. 1 of Duru et al. (2006). Copyright 2006 American Geophysical Union. Reproduced by permission of American Geophysical Union.

Nielsen et al. (2007c) and Gurnett et al. (2008) hypothesized that enhanced topside electron densities above strong and vertical magnetic fields are caused by high electron temperatures. They suggested that electrons are heated in regions of strong and vertical magnetic field by the influx of solar wind plasma along open fieldlines. In this case, unlike Section 5.4, the high electron temperatures increase plasma densities through their effect on the vertical transport of plasma by diffusion, not by their effect on α, the dissociative recombination coefficient (Rishbeth and Garriott, 1969).

7.4. Topside layering and structure

As shown in Fig. 36, some MARSIS electron density profiles contain a region around 160–180 km where electron densities exceed the background trend and form a bulge. Other examples can be seen in Nielsen et al. (2006). Similar features in Mars Express radio occultation profiles were reported by Pätzold et al. (2007). These altitudes are below the transport-dominated region of the topside ionosphere, so these features are created by photochemical processes (Nagy and Cravens, 2002). The origin of these features has not yet been explained.

MARSIS AIS mode ionograms reported in Kopf et al. (2008) and Gurnett et al. (2008) show a "second layer" at

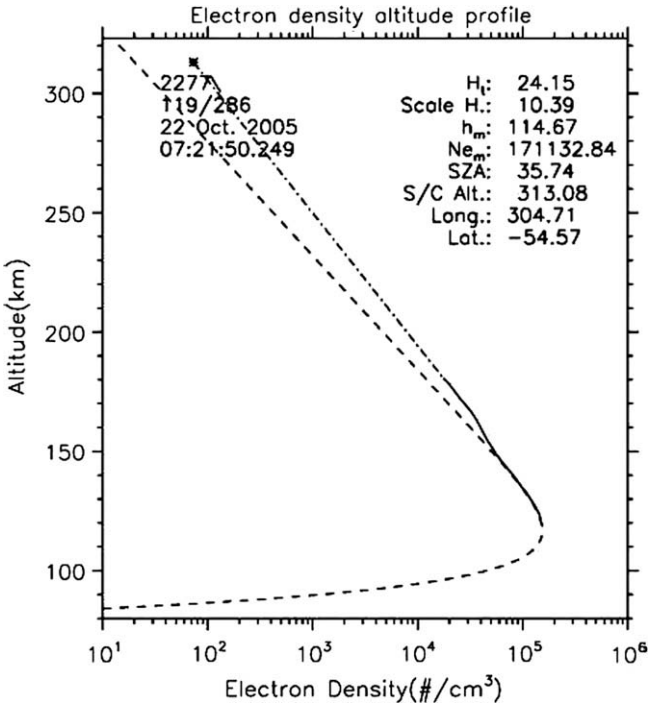

Fig. 36. Electron density profile (solid line) obtained by the AIS mode of the MARSIS instrument on orbit 2277. The asterisk indicates the electron density at the spacecraft inferred from electron plasma oscillations (Duru et al., 2008). The dot–dash line indicates the assumed electron density between the spacecraft and the top of the detected ionosphere. The dashed line is a Chapman fit to the solid line. Reproduced from Fig. 7 of Nielsen et al. (2006). With kind permission of Springer Science and Business Media: Fig. 7 of Nielsen et al. (2006).

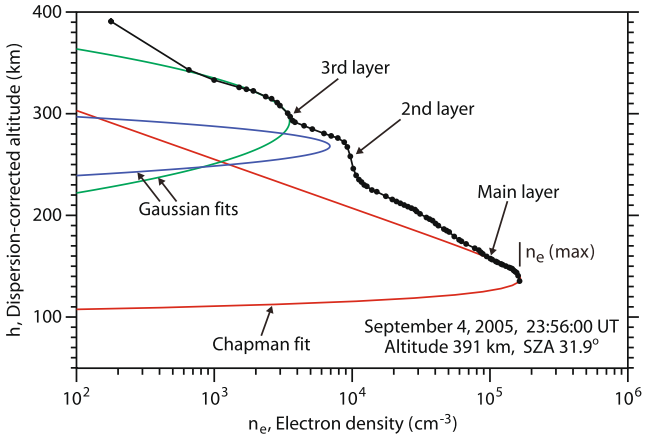

Fig. 37. An electron density profile (dots joined by solid line) obtained by the AIS mode of the MARSIS instrument. The red line is a Chapman fit to the electron density profile near the M2 layer. The blue and green lines are Gaussian fits to the arrowed second and third topside layers, respectively. Reproduced from Fig. 5 of Kopf et al. (2008). Copyright 2008 American Geophysical Union. Reproduced by permission of American Geophysical Union. (For interpretation of colour mentioned in this figure caption the reader is referred to the web version of the article.)

apparent ranges that are stated to be equivalent to altitudes "above about 200 km". The one electron density profile shown in these two papers that contains this layer places it at 270 km, as shown in Fig. 37, well above the bulge at 160–180 km. In this example, a "third layer", which only occurs in 1% of MARSIS AIS mode observations, is also present at even higher altitudes (Kopf et al., 2008). Layer thicknesses are tens of kilometres. Kopf et al. (2008) reported that the occurrence rate of this "second layer" is about 60% near the subsolar point and decreases with increasing SZA to <5% at the terminator. Kopf et al. (2008) suggested that these layers are produced by a dynamical process involving an interaction with the solar wind.

Wang and Nielsen (2003) investigated wavelike structures in the topside ionosphere using MGS radio occultation electron density profiles. They classified electron density profiles into five types based upon the waviness of the topside ionosphere, identified a dominant wavelength of ≈40 km, and interpreted these observations as waves in the ionosphere excited by solar wind pressure.

7.5. The upper boundary of the dayside ionosphere

A novel application of the MARSIS AIS mode was explored by Duru et al. (2008). MARSIS is able to measure "*in situ* electron density from the excitation of local plasma oscillations", as shown in Fig. 38. Electron densities were measured between 275 km and 1300 km over SZAs from 0° to 150°. Composite vertical profiles of electron density within a narrow SZA range were then assembled from the available data. Dayside plasma scale heights, which were found to be on the order of 100 km, increase as SZA increases. Electron density at fixed altitude is constant for small SZAs, then decreases with increasing SZA above

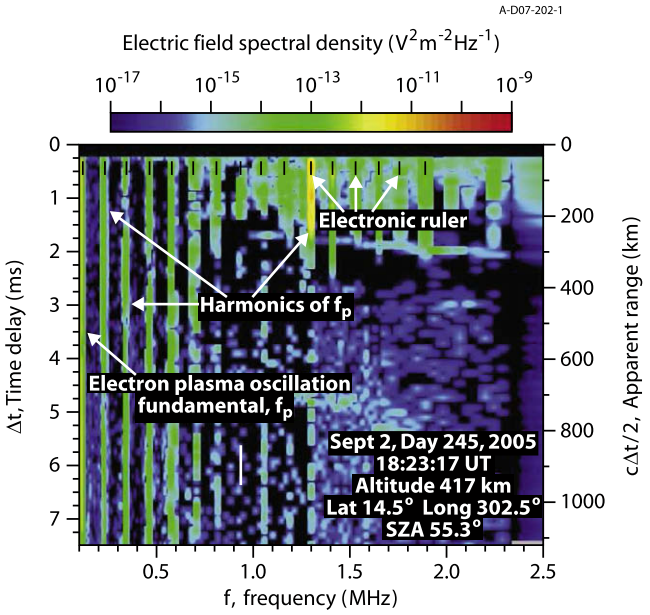

Fig. 38. An ionogram obtained by the AIS mode of the MARSIS instrument that shows harmonics of electron plasma oscillations in the local plasma. The local electron density can be determined from the fundamental frequency of these oscillations. Reproduced from Fig. 2 of Duru et al. (2008). Copyright 2008 American Geophysical Union. Reproduced by permission of American Geophysical Union.

some threshold SZA. The threshold SZA, which is approximately 80° at 250–300 km, increases as altitude increases. These oscillations are not detectable in hot, tenuous solar wind plasma, but are detectable in ionospheric plasma denser than 10 cm^{-3}. Hence a boundary between ionospheric plasma and shocked solar wind plasma can be identified using MARSIS AIS mode observations of these plasma oscillations. The altitude of this boundary increases with SZA from 700 km at SZA = 0° to 1200 km at SZA = 90°.

The upper boundary of the dayside ionosphere was also studied by Mitchell et al. (2001). The MGS Electron Reflectometer measures electron fluxes and densities as a function of energy. Mitchell et al. (2001) identified a boundary at an average altitude of 400 km based upon electron energy spectra. Below this boundary, the spectra contain relatively high electron densities at 10–60 eV, the energy range of photoelectrons, and at 500 eV, the energy of Auger electrons from atomic oxygen, as shown in Fig. 39 (Mitchell et al., 2000). Above this boundary, the electron energy spectrum is not peaked. Clearly, the boundaries identified by Duru et al. (2008) and Mitchell et al. (2001) are different.

The interaction between the dayside martian atmosphere/ionosphere and the solar wind is complex. Consequently, the martian plasma environment contains multiple regions and boundaries, as shown in Fig. 40 (Crider et al., 2003; Nagy et al., 2004; Brain, 2006; Dubinin et al., 2008). The most distant dayside boundary is the bow shock, the point at which solar wind decelerates upon encountering the planetary obstacle, and unshocked solar wind plasma lies outside the bow shock. The region enclosed by the bow shock is called the magnetosheath and it contains shocked, turbulent, high temperature solar wind plasma. A boundary called the magnetic pileup boundary (MPB) separates this shocked solar wind plasma (predominantly hydrogen and helium ions) in the magnetosheath from plasma of ionospheric origin (predominantly heavier ions such as oxygen) in the magnetic pileup region (MPR). The boundary identified by Mitchell et al. (2001), subsequently called the photoelectron boundary (PEB), separates plasma of ionospheric origin whose electron energy spectrum has lost the distinctive features of its origin in photoionization processes from "pure" ionospheric plasma at lower altitudes whose electron energy spectrum retains those features. Typical altitudes of these three boundaries at the subsolar point are 2000 km for the bow shock, 850 km for the magnetic pileup boundary, and 400 km for the photoelectron boundary (Mitchell et al., 2001; Brain, 2006). If the boundary mapped by Duru et al. (2008) corresponds to any one of these three, then it is most likely the magnetic pileup boundary.

The study of the martian plasma environment above the exobase is currently thriving due to extensive measurements by the Mars Express ASPERA, MGS magnetometer and MGS Electron Reflectometer instruments (Acuña et al., 2001; Mitchell et al., 2001; Barabash et al., 2006). Recent observational papers on this topic include Crider et al. (2004), Krymskii et al. (2004), Lundin and Barabash (2004), Brain (2006) and Dubinin et al. (2008); recent theoretical papers include Ma et al. (2004), Brecht and Ledvina (2006), Harnett and Winglee (2006), Kallio et al. (2006) and Kaneda et al. (2007); and recent special issues include ISSI (2004) and Russell (2006). Further discussion of the upper boundary, or boundaries, of the ionosphere is outside the scope of the current paper, and the reader is directed to the recent review articles of Nagy et al. (2004) and Brain (2006) for more comprehensive analyses.

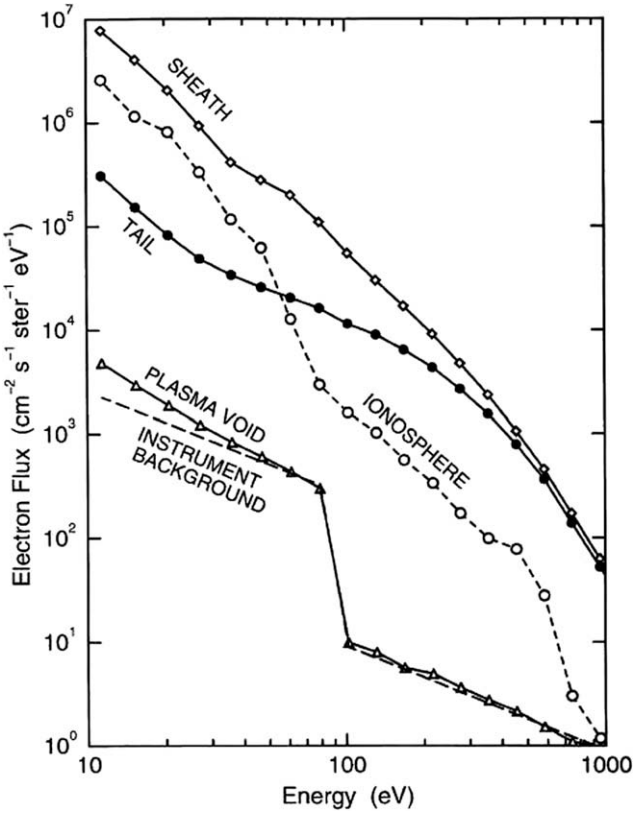

Fig. 39. Typical electron energy spectra measured by the MGS Electron Reflectometer in different regions. Open diamonds indicate the magnetosheath, open circles indicate the ionosphere, solid disks indicate the magnetotail, and open triangles indicate plasma voids. The instrument background is shown by dashed lines. Plasma voids occur in the geometric shadow of Mars and "are closely associated with crustal magnetic sources" (Mitchell et al., 2001). Mitchell et al. (2001) inferred that plasma voids lie on closed crustal field lines and are isolated from both solar wind plasma and dayside ionospheric plasma. Ionospheric plasma is characterized by relatively high plasma densities at 10–60 eV, the energy range of photoelectrons, and at 500 eV, the energy of Auger electrons from atomic oxygen (Mitchell et al., 2000). Reproduced from Fig. 7 of Mitchell et al. (2000). Copyright 2001 American Geophysical Union. Reproduced by permission of American Geophysical Union.

8. Predicted variability in ionospheric chemistry and electrodynamics

There are no observations of plasma dynamics in the martian ionosphere. When observations become available in the future, they are likely to show plasma flow across the terminator, upward flow of plasma in the topside ion-

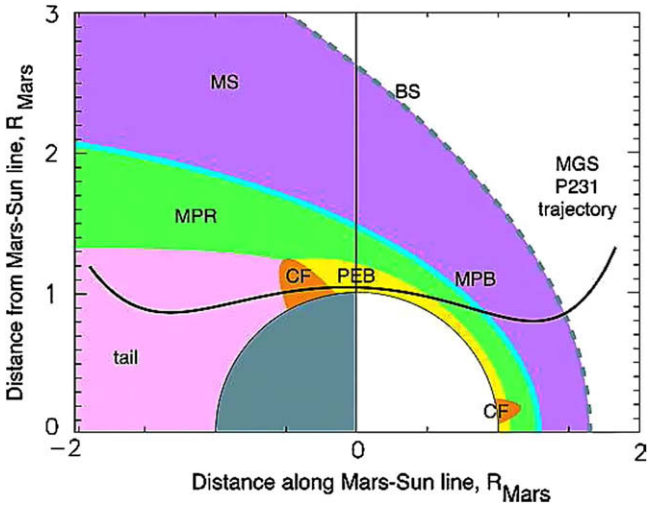

Fig. 40. An idealized sketch of the structure of the martian plasma environment. The Sun's position is far along the horizontal axis to the right. The shaded areas represent the bow shock (BS, dashed line), magnetosheath (MS, purple), magnetic pileup boundary (MPB, blue), magnetic pileup region (MPR, green), photoelectron boundary and ionosphere (PEB, yellow), regions strongly influenced by crustal fields (CF, orange), and the magnetotail (tail, pink). Also shown is the trajectory of MGS on orbit P231. This figure omits the nightside ionosphere, which is poorly characterized. Reproduced from Fig. 1 of Crider et al. (2003). Copyright 2003 American Geophysical Union. Reproduced by permission of American Geophysical Union. (For interpretation of colour mentioned in this figure caption the reader is referred to the web version of the article.)

osphere, sensitivity of three-dimensional bulk motion of plasma to magnetic field strength and direction, and sensitivity of small-scale plasma instabilities to magnetic field strength and direction. All these aspects of plasma dynamics will exhibit variations.

There are very few observations of the chemical composition of the neutral upper atmosphere and ionosphere, which are also likely to exhibit variations. The most abundant constituents are O and CO_2. Models predict variations in the O/CO_2 ratio with altitude, local solar time and solar cycle that will affect ionospheric properties (Bougher et al., 1999). The composition of the topside ionosphere remains an open question. Viking RPA data always show O_2^+ as more abundant than O^+, even at 300 km (Nier and McElroy, 1977). Experience from Venus, whose dayside ionosphere is very similar to that of Mars, suggests that O^+ should eventually become the most abundant species (Brace et al., 1983). Some models predict that O^+ becomes the most abundant species at high altitudes (Shinagawa and Cravens, 1989; Shinagawa and Cravens, 1992; Winchester and Rees, 1995; Ma et al., 2004), yet other models predict that O_2^+ remains the most abundant species (Chen et al., 1978; Fox et al., 1996; Krasnopolsky, 2002; Fox, 2004b).

Trace species may also affect the ionosphere. Meteoric plasma layers are produced by small amounts of metallic species deposited in the atmosphere by meteoroids. Their chemistry is thought to be dominated by metallic ions, such as Mg^+ and $Mg^+{\cdot}CO_2$ (Pesnell and Grebowsky, 2000; Molina-Cuberos et al., 2003). However, there are no observations of the chemical composition of meteoric layers, or of interactions between metallic species and common ions (e.g., CO_2^+ and O_2^+). The only direct measurement of metallic species is an observation of two infra-red emission features from $Mg^+{\cdot}CO_2$ (Aikin and Maguire, 2005; Maguire and Aikin, 2006). Some models suggest that densities of nitrogen-bearing ions, such as NO^+, are $10^4\,cm^{-3}$ at 100 km, making them a major ionospheric constituent at altitudes close to the M1 layer (Chen et al., 1978; Krasnopolsky, 2002; Fox, 2004b). Other models either suggest that nitrogen-bearing ions are negligible at all altitudes (Winchester and Rees, 1995; Fox et al., 1996) or do not include any nitrogen-bearing ions (Shinagawa and Cravens, 1989; Shinagawa and Cravens, 1992; Ma et al., 2004). Given the current paucity of observations of neutral and ionic composition, it might also be prudent to consider the possibility that other trace species, as yet undetected, may play important roles in ionospheric chemistry.

9. Conclusions

The martian dayside ionosphere can be divided into three regions — the M2 layer, below the M2 layer, and above the M2 layer. The M2 layer is often represented as a Chapman layer. It is produced by the photoionization of CO_2 molecules by solar EUV photons and is dominated by O_2^+ ions. The region below the M2 layer contains the M1 layer, the meteoric layer, and a poorly-constrained plasma reservoir at lower altitudes. The M1 layer is produced by the photoionization of CO_2 molecules by solar X-ray photons and subsequent electron-impact ionization, and is also dominated by O_2^+ ions. Only ~10% of ion–electron pairs in the M1 layer are produced by photoionization. The meteoric layer is sporadically present, is produced by the ablation of meteoroids, and its dominant ion species have not been measured. There is evidence for an additional plasma reservoir below the M2 layer that is produced by energetic particles. The region above the M2 layer is characterized by the growing importance of O, O^+ and transport processes.

The foremost characteristics of the M2 layer are its altitude, width and electron density. Most variations in these characteristics are accurately described by quantitative predictions from Chapman theory. The dependences of N_m and z_m on SZA are consistent with Chapman theory, and the values of the subsolar peak electron density and subsolar peak altitude are consistent with theoretical predictions. However, the observed dependence between peak electron density and solar irradiance is not as strong as predicted by Chapman theory. The reason for this discrepancy is not clear, but inadequate proxies for ionizing flux and difficulties in accounting for variations in H and α are possibilities. Periodic variations in peak electron density have been related to changes in solar irradiance at Mars caused by the rotation of the Sun, whose irradiance is inhomogeneous across its disk. More rapid variations in peak elec-

tron density with time are caused by solar flares. Dawn–dusk asymmetries in electron density are present, although their cause has not been identified. Measurements of the width and altitude of the M2 layer can be used to characterize the neutral atmosphere, although the width of the M2 layer has been underutilized in existing work. The peak altitude has been used to characterize thermal tides and the thermal state of the lower atmosphere. Enhanced peak electron densities are found in regions with strong and vertical magnetic fields. These have been attributed to electron heating along open fieldlines due to a two-stream plasma instability.

The M1 layer is hard to measure because it often appears as a perturbation to the bottom of the M2 layer that is relatively small in comparison to the uncertainties in radio occultation measurements. The electron density profile in the M1 layer cannot be measured by the MARSIS instrument as it is below the M2 layer. Models have not reproduced the detailed characteristics of the M1 layer well. The M1 layer varies on short timescales due to temporal variations in solar X-ray flux. Peak electron densities in the M1 layer are proportional to the square root of the cosine of SZA, consistent with theoretical expectations for the photochemical region of an ionosphere where the dominant loss process is the dissociative recombination of molecular ions. Occasionally, electron densities in the M1 layer are atypically small. The M1 layer responds strongly to solar flares. Electron densities increase throughout the M1 layer during a solar flare, and the relative increase in electron density increases as altitude decreases, consistent with the hardening of the solar spectrum during a solar flare. Radio occultation electron density profiles sometimes show an additional layer at 80–100 km, below the M1 layer. This is produced by meteoroid ablation. Its occurrence rate varies strongly with season, consistent with control by variations in meteoroid flux. The altitude, width and electron density of the meteoric layer are positively correlated, but they are not strongly correlated with solar irradiance or SZA. The MARSIS instrument fails to detect reflections from the ground during energetic particle events, which suggests that plasma is being produced somewhere below the M2 layer by these energetic particles. Theorists have also predicted that cosmic rays should maintain a reservoir of plasma with electron densities in excess of $100\,cm^{-3}$ at 35 km.

Above the M2 layer, the topside ionosphere is influenced by the solar wind and by whether magnetic fieldlines connect the ionosphere to the solar wind or not. Some MGS radio occultation profiles measured over strong crustal magnetic fields contain localized increases or decreases in topside electron density. Their cause is unknown. Mars Express radio occultation electron density profiles consistently contain a bulge in electron density at 160–180 km and MARSIS data regularly indicate ionospheric layering above 200 km. *In situ* MARSIS measurements of electron density, which have been used to construct composite electron density profiles from 275 km to 1200 km, have mapped a boundary between the ionosphere and solar wind, finding that its altitude increases from 700 km at SZA = 0° to 1200 km at SZA = 90°.

Variations in ionospheric chemistry and plasma dynamics are expected, but have not yet been observed. Both ionospheric chemistry and plasma dynamics have substantial effects on the structure and properties of the ionosphere.

In summary, the martian dayside ionosphere exhibits variability in many ways. The physical characteristics of persistent features of the dayside ionosphere, which include the M1 layer, M2 layer and topside, vary. Other ionospheric features, such as the meteoric layer and plasma produced by solar energetic particles, are only detectable sporadically. Ionospheric properties are sensitive to changes in solar irradiance, SZA, magnetic field strength, direction and topology, meteoroid flux, and the neutral atmosphere.

The basic physical and chemical processes that control planetary ionospheres are the same on all solar system bodies — the conservation laws of mass, momentum and energy govern ionospheric chemistry, dynamics and energetics, respectively (Mendillo et al., 2002). The state of an ionosphere results from the application of these general principles in the specific conditions of one planetary environment. Comparative studies of ionospheric processes and properties are valuable for revealing which aspects of ionospheric behaviour are specific to a given planetary environment and which are more general. The following four examples illustrate this point. Slowly-rotating Venus has a denser nightside ionosphere than rapidly-rotating Mars, despite their similar ionospheric chemistries, due to intense upper atmospheric circulation from the subsolar region to the anti-solar region. Earth and Jupiter have similar rotation rates and magnetic fields, but differences in chemical composition produce strikingly different layering in their electron density profiles. Titan and Triton have similar nitrogen–methane compositions in their bulk atmospheres, and solar irradiance is an order of magnitude stronger at Titan than Triton, yet ionospheric plasma densities are an order of magnitude smaller at Titan than Triton due to small amounts of complex hydrocarbons present only in the atmosphere of Titan. The chemical compositions of the ionospheres of Enceladus and comet Halley are similar, dominated by ions derived from water molecules, but the vertical extent of the cometary ionosphere is much greater due to the weak cometary gravity.

Comparative studies investigate how ionospheric properties change in response to variations in planetary size, chemical composition, rotation rate or global-scale magnetic topology and strength, which are natural developments of the studies of how ionospheric properties change with variations in solar zenith angle, solar irradiance or local magnetic field structure summarized in this paper. Indeed, comparative aeronomy can be viewed as a powerful extension of studies of variability. The acknowl-

edged value of comparative aeronomy is a reminder that its precursor, single-planet studies of variability, is also a capable tool. When observed variations in some ionospheric property are successfully explained by a model, there are always residual differences between the model and observations. These residuals, small though they may be in comparison to the original variations, constitute the new variations whose existence and behaviour must be explained and simulated.

Acknowledgements

This paper is based on presentation C32-0011-08 from the 2008 COSPAR Scientific Assembly (Withers, 2008). P.W. acknowledges two anonymous reviewers for valuable comments that immeasurably improved this paper and doubled its length, helpful discussions with Michael Mendillo, and support from NASA Grants NNX07AN99G and NNX08AN56G.

References

Acuña, M.H., Connerney, J.E.P., Ness, N.F., Lin, R.P., Mitchell, D., Carlson, C.W., McFadden, J., Anderson, K.A., Rème, H., Mazelle, C., Vignes, D., Wasilewski, P., Cloutier, P. Global distribution of crustal magnetization discovered by the Mars Global Surveyor MAG/ER Experiment. Science 284, 790–793, 1999.

Acuña, M.H., Connerney, J.E.P., Wasilewski, P., Lin, R.P., Mitchell, D., Anderson, K.A., Carlson, C.W., McFadden, J., Rème, H., Mazelle, C., Vignes, D., Bauer, S.J., Cloutier, P., Ness, N.F. Magnetic field of Mars: summary of results from the aerobraking and mapping orbits. J. Geophys. Res. 106, 23403–23418, 2001.

Aikin, A.C., Maguire, W.C. Detection in the infrared of $Mg^{+}{\cdot}CO_2$ ion produced via meteoritic material in the martian atmosphere. Am. Astron. Soc. DPS Meeting 37, 33.37, 2005.

Arkani-Hamed, J. A coherent model of the crustal magnetic field of Mars. J. Geophys. Res. 109, E09005, doi:10.1029/2004JE002265, 2004.

Banks, P.M., Kockarts, G.. Aeronomy. Academic Press, New York, 1973.

Barabash, S., Lundin, R., Andersson, H., Brinkfeldt, K., Grigoriev, A., Gunell, H., Holmström, M., Yamauchi, M., Asamura, K., Bochsler, P., Wurz, P., Cerulli-Irelli, R., Mura, A., Milillo, A., Maggi, M., Orsini, S., Coates, A.J., Linder, D.R., Kataria, D.O., Curtis, C.C., Hsieh, K.C., Sandel, B.R., Frahm, R.A., Sharber, J.R., Winningham, J.D., Grande, M., Kallio, E., Koskinen, H., Riihelä, P., Schmidt, W., Säles, T., Kozyra, J.U., Krupp, N., Woch, J., Livi, S., Luhmann, J.G., McKenna-Lawlor, S., Roelof, E.C., Williams, D.J., Sauvaud, J.-A., Fedorov, A., Thocaven, J.-J. The analyzer of space plasmas and energetic atoms (ASPERA-3) for the Mars Express mission. Space Sci. Rev. 126, 113–164, 2006.

Barth, C.A., Stewart, A.I.F., Bougher, S.W., Hunten, D.M., Bauer, S.J., Nagy, A.F. Aeronomy of the current martian atmosphere, in: Kieffer, H.H., Jakosky, B.M., Snyder, C.W., Matthews, M.S. (Eds.), Mars. University of Arizona Press, Arizona, pp. 1054–1089, 1992.

Bertucci, C., Mazelle, C., Crider, D.H., Vignes, D., Acuña, M.H., Mitchell, D.L., Lin, R.P., Connerney, J.E.P., Rème, H., Cloutier, P.A., Ness, N.F., Winterhalter, D. Magnetic field draping enhancement at the Martian magnetic pileup boundary from Mars Global Surveyor observations. Geophys. Res. Lett. 30, 1099, doi:10.1029/2002GL015713, 2003.

Bevington, P.R. Data Reduction and Error Analysis for the Physical Sciences, first ed Cambridge University Press, New York, 1969.

Bougher, S., Engel, S., Roble, R.G., Foster, B. Comparative terrestrial planet thermospheres 2. Solar cycle variation of global structure and winds at equinox. J. Geophys. Res. 104, 16591–16611, 1999.

Bougher, S.W., Engel, S., Hinson, D.P., Forbes, J.M. Mars Global Surveyor Radio Science electron density profiles: neutral atmosphere implications. Geophys. Res. Lett. 28, 3091–3094, 2001.

Bougher, S.W., Engel, S., Hinson, D.P., Murphy, J.R. MGS radio science electron density profiles: interannual variability and implications for the martian neutral atmosphere. J. Geophys. Res. 109, E03010, doi:10.1029/2003JE002154, 2004.

Brace, L.H., Taylor, H.A., Gombosi, T.I., Kliore, A.J., Knudsen, W.C., Nagy, A.F. The ionosphere of Venus: observations and their interpretations, in: Hunten, D.M., Colin, L., Donahue, T.M., Moroz, V.I. (Eds.), Venus. University of Arizona Press, Arizona, pp. 779–840, 1983.

Brain, D.A. Mars Global Surveyor measurements of the martian solar wind interaction. Space Sci. Rev. 126, 77–112, 2006.

Brain, D.A., Bagenal, F., Acuña, M.H., Connerney, J.E.P. Martian magnetic morphology: contributions from the solar wind and crust. J. Geophys. Res. 108, 1424, doi:10.1029/2002JA009482, 2003.

Brain, D.A., Lillis, R.J., Mitchell, D.L., Halekas, J.S., Lin, R.P. Electron pitch angle distributions as indicators of magnetic field topology near Mars. J. Geophys. Res. 112, A09201, doi:10.1029/2007JA012435, 2007.

Brecht, S.H., Ledvina, S.A. The solar wind interaction with the martian ionosphere/atmosphere. Space Sci. Rev. 126, 15–38, 2006.

Breus, T.K., Krymskii, A.M., Crider, D.H., Ness, N.F., Hinson, D., Barashyan, K.K. Effect of the solar radiation in the topside atmosphere/ionosphere of Mars: Mars Global Surveyor observations. J. Geophys. Res. 109, A09310, doi:10.1029/2004JA010431, 2004.

Cain, J.C., Ferguson, B.B., Mozzoni, D. An $n = 90$ internal potential function of the martian crustal magnetic field. J. Geophys. Res. 108, 5008, doi:10.1029/2000JE001487, 2003.

Chamberlain, J.W., Hunten, D.M. Theory of Planetary Atmospheres. second ed.. Academic Press, New York, 1987.

Chapman, S. The absorption and dissociative or ionizing effect of monochromatic radiation in an atmosphere on a rotating Earth. Proc. Phys. Soc. 43, 26–45, 1931a.

Chapman, S. The absorption and dissociative or ionizing effect of monochromatic radiation in an atmosphere on a rotating Earth. Part II. Grazing incidence. Proc. Phys. Soc. 43, 483–501, 1931b.

Chen, R.H., Cravens, T.E., Nagy, A.F. The martian ionosphere in light of the Viking observations. J. Geophys. Res. 83, 3871–3876, 1978.

Christou, A.A., Vaubaillon, J., Withers, P. The dust trail complex of 79P/du Toit–Hartley and meteor outbursts at Mars. Astron. Astrophys. 471, 321–329, 2007.

Crider, D.H., Acuña, M.H., Connerney, J.E.P., Vignes, D., Ness, N.F., Krymskii, A.M., Breus, T.K., Rème, H., Mazelle, C., Mitchell, D.L., Lin, R.P., Cloutier, P.A., Winterhalter, D. Observations of the latitude dependence of the location of the martian magnetic pileup boundary. Geophys. Res. Lett. 29, 1170, doi:10.1029/2001GL013860, 2002.

Crider, D.H., Brain, D.A., Acuña, M.H., Vignes, D., Mazelle, C., Bertucci, C. Mars Global Surveyor observations of solar wind magnetic field draping around Mars. Space Sci. Rev. 111, 203–221, 2004.

Crider, D.H., Vignes, D., Krymskii, A.M., Breus, T.K., Ness, N.F., Mitchell, D.L., Slavin, J.A., Acuña, M.H. A proxy for determining solar wind dynamic pressure at Mars using Mars Global Surveyor data. J. Geophys. Res. 108, 1461, doi:10.1029/2003JA009875, 2003.

Dubinin, E., Modolo, R., Fraenz, M., Woch, J., Chanteur, G., Duru, F., Akalin, F., Gurnett, D., Lundin, R., Barabash, S., Winningham, J.D., Frahm, R., Plaut, J.J., Picardi, G. Plasma environment of Mars as observed by simultaneous MEX-ASPERA-3 and MEX-MARSIS observations. J. Geophys. Res. 113, A10217, doi:10.1029/2008JA013355, 2008.

Duru, F., Gurnett, D.A., Averkamp, T.F., Kirchner, D.L., Huff, R.L., Persoon, A.M., Plaut, J.J., Picardi, G. Magnetically controlled structures in the ionosphere of Mars. J. Geophys. Res. 111, A12204, doi:10.1029/2006JA011975, 2006.

Duru, F., Gurnett, D.A., Morgan, D.D., Modolo, R., Nagy, A.F., Najib, D. Electron densities in the upper ionosphere of Mars from the

excitation of electron plasma oscillations. J. Geophys. Res. 113, A07302, doi:10.1029/2008JA013073, 2008.
Espley, J.R., Farrell, W.M., Brain, D.A., Morgan, D.D., Cantor, B., Plaut, J.J., Acuña, M.H., Picardi, G. Absorption of MARSIS radar signals: solar energetic particles and the daytime ionosphere. Geophys. Res. Lett. 34, L09101, doi:10.1029/2006GL028829, 2007.
Fjeldbo, G., Kliore, A.J., Eshleman, V.R. The neutral atmosphere of Venus as studied with the Mariner V radio occultation experiments. Astron. J. 76, 123–140, 1971.
Forbes, J.M., Bridger, A.F.C., Bougher, S.W., Hagan, M.E., Hollingsworth, J.L., Keating, G.M., Murphy, J. Nonmigrating tides in the thermosphere of Mars. J. Geophys. Res. 107, 5113, doi:10.1029/2001JE001582, 2002.
Fox, J.L. Advances in the aeronomy of Venus and Mars. Adv. Space Res. 33, 132–139, 2004a.
Fox, J.L. Response of the martian thermosphere/ionosphere to enhanced fluxes of solar soft X-rays. J. Geophys. Res. 109, A11310, doi:10.1029/2004JA010380, 2004b.
Fox, J.L., Brannon, J.F., Porter, H.S. Upper limits to the nightside ionosphere of Mars. Geophys. Res. Lett. 20, 1339–1342, 1993.
Fox, J.L., Yeager, K.E. Morphology of the near-terminator martian ionosphere: a comparison of models and data. J. Geophys. Res. 111, A10309, doi:10.1029/2006JA011697, 2006.
Fox, J.L., Zhou, P., Bougher, S.W. The martian thermosphere/ionosphere at high and low solar activities. Adv. Space Res. 17, 203–218, 1996.
Gurnett, D.A., Huff, R.L., Morgan, D.D., Persoon, A.M., Averkamp, T.F., Kirchner, D.L., Duru, F., Akalin, F., Kopf, A.J., Nielsen, E., Safaeinili, A., Plaut, J.J., Picardi, G. An overview of radar soundings of the martian ionosphere from the Mars Express spacecraft. Adv. Space Res. 41, 1335–1346, 2008.
Gurnett, D.A., Kirchner, D.L., Huff, R.L., Morgan, D.D., Persoon, A.M., Averkamp, T.F., Duru, F., Nielsen, E., Safaeinili, A., Plaut, J.J., Picardi, G. Radar soundings of the ionosphere of Mars. Science 310, 1929–1933, 2005.
Hanson, W.B., Mantas, G.P. Viking electron temperature measurements — evidence for a magnetic field in the martian ionosphere. J. Geophys. Res. 93, 7538–7544, 1988.
Hanson, W.B., Sanatani, S., Zuccaro, D.R. The martian ionosphere as observed by the Viking retarding potential analyzers. J. Geophys. Res. 82, 4351–4363, 1977.
Hantsch, M.H., Bauer, S.J. Solar control of the Mars ionosphere. Planet. Space Sci. 38, 539–542, 1990.
Harnett, E.M., Winglee, R.M. Three-dimensional multifluid simulations of ionospheric loss at Mars from nominal solar wind conditions to magnetic cloud events. J. Geophys. Res. 111, A09213, doi:10.1029/2006JA011724, 2006.
Hinson, D.P., Simpson, R.A., Twicken, J.D., Tyler, G.L., Flasar, F.M. Initial results from radio occultation measurements with Mars Global Surveyor. J. Geophys. Res. 104, 26997–27012, 1999.
Hinson, D.P., Simpson, R.A., Twicken, J.D., Tyler, G.L., Flasar, F.M. Erratum: initial results from radio occultation measurements with Mars Global Surveyor. J. Geophys. Res. 105, 1717–1718, 2000.
ISSI. Volume contents. Space Sci. Rev. 111, 481–482, 2004.
Kallio, E., Fedorov, A., Barabash, S., Janhunen, P., Koskinen, H., Schmidt, W., Lundin, R., Gunell, H., Holmström, M., Futaana, Y., Yamauchi, M., Grigoriev, A., Winningham, J.D., Frahm, R., Sharber, J.R. Energisation of O^+ and O_2^+ ions at Mars: an analysis of a 3-D quasi-neutral hybrid model simulation. Space Sci. Rev. 126, 39–62, 2006.
Kallio, E., Janhunen, P. Atmospheric effects of proton precipitation in the martian atmosphere and its connection to the Mars–solar wind interaction. J. Geophys. Res. 106, 5617–5634, 2001.
Kaneda, K., Terada, N., Machida, S. Time variation of nonthermal escape of oxygen from Mars after solar wind dynamic pressure enhancement. Geophys. Res. Lett. 34, L20201, doi:10.1029/2007GL030576, 2007.
Keating, G.M., Bougher, S.W., Zurek, R.W., Tolson, R.H., Cancro, G.J., Noll, S.N., Parker, J.S., Schellenberg, T.J., Shane, R.W., Wilkerson, B.L., Murphy, J.R., Hollingsworth, J.L., Haberle, R.M., Joshi, M., Pearl, J.C., Conrath, B.J., Smith, M.D., Clancy, R.T., Blanchard, R.C., Wilmoth, R.G., Rault, D.F., Martin, T.Z., Lyons, D.T., Esposito, P.B., Johnston, M.D., Whetzel, C.W., Justus, C.G., Babicke, J.M. The structure of the upper atmosphere of Mars: in situ accelerometer measurements from Mars Global Surveyor. Science 279, 1672–1676, 1998.
Kliore, A.J. Radio occultation observations of the ionospheres of Mars and Venus, in: Venus and Mars: Atmospheres, Ionospheres, and Solar Wind Interactions. Geophysical Monograph Series, vol. 66. American Geophysical Union, Washington, DC, pp. 265–276, 1992.
Kopf, A.J., Gurnett, D.A., Morgan, D.D., Kirchner, D.L. Transient layers in the topside ionosphere of Mars. Geophys. Res. Lett. 35, L17102, doi:10.1029/2008GL034948, 2008.
Krasnopolsky, V.A. Mars' upper atmosphere and ionosphere at low, medium, and high solar activities: implications for evolution of water. J. Geophys. Res. 107, 5128, doi:10.1029/2001JE001809, 2002.
Krymskii, A.M., Breus, T.K., Ness, N.F., Hinson, D.P., Bojkov, D.I. Effect of crustal magnetic fields on the near terminator ionosphere at Mars: comparison of in situ magnetic field measurements with the data of radio science experiments on board Mars Global Surveyor. J. Geophys. Res. 108, 1431, doi:10.1029/2002JA009662, 2003.
Krymskii, A.M., Ness, N.F., Crider, D.H., Breus, T.K., Acuña, M.H., Hinson, D.P. Solar wind interaction with the ionosphere/atmosphere and crustal magnetic fields at Mars: Mars Global Surveyor magnetometer/electron reflectometer, radio science, and accelerometer data. J. Geophys. Res. 109, A11306, doi:10.1029/2004JA010420, 2004.
Langlais, B., Purucker, M.E., Mandea, M. Crustal magnetic field of Mars. J. Geophys. Res. 109, E02008, doi:10.1029/2003JE002048, 2004.
Leblanc, F., Luhmann, J.G., Johnson, R.E., Chassefiere, E. Some expected impacts of a solar energetic particle event at Mars. J. Geophys. Res. 107, 1058, doi:10.1029/2001JA900178, 2002.
Lide, D.R. CRC Handbook of Chemistry and Physics, 75th ed CRC Press, Boca Raton, FL, 1994.
Lillis, R.J., Frey, H.V., Manga, M., Mitchell, D.L., Lin, R.P., Acuña, M.H., Bougher, S.W. An improved crustal magnetic field map of Mars from electron reflectometry: highland volcano magmatic history and the end of the martian dynamo. Icarus 194, 575–596, 2008.
Lundin, R., Barabash, S. Evolution of the martian atmosphere and hydrosphere: solar wind erosion studied by ASPERA-3 on Mars Express. Planet. Space Sci. 52, 1059–1071, 2004.
Ma, Y., Nagy, A.F., Sokolov, I.V., Hansen, K.C. Three-dimensional, multispecies, high spatial resolution MHD studies of the solar wind interaction with Mars. J. Geophys. Res. 109, A07211, doi:10.1029/2003JA010367, 2004.
Maguire, W.C., Aikin, A.C. Infrared signature of meteoritic material in the martian atmosphere from MGS/TES limb observations. Am. Astron. Soc. DPS Meeting 38, 23.60, 2006.
Martinis, C.R., Wilson, J.K., Mendillo, M.J. Modeling day-to-day ionospheric variability on Mars. J. Geophys. Res. 108, 1383, doi:10.1029/2003JA009973, 2003.
Mendillo, M., Nagy, A., Waite, J.H. Atmospheres in the Solar System: Comparative Aeronomy. American Geophysical Union, Washington, DC, 2002.
Mendillo, M., Smith, S., Wroten, J., Rishbeth, H., Hinson, D. Simultaneous ionospheric variability on Earth and Mars. J. Geophys. Res. 108, 1432, doi:10.1029/2003JA009961, 2003.
Mendillo, M., Withers, P., Hinson, D., Rishbeth, H., Reinisch, B. Effects of solar flares on the ionosphere of Mars. Science 311, 1135–1138, 2006.
Mitchell, D.L., Lin, R.P., Mazelle, C., Rème, H., Cloutier, P.A., Connerney, J.E.P., Acuña, M.H., Ness, N.F. Probing Mars' crustal magnetic field and ionosphere with the MGS electron reflectometer. J. Geophys. Res. 106, 23419–23428, 2001.
Mitchell, D.L., Lin, R.P., Rème, H., Crider, D.H., Cloutier, P.A., Connerney, J.E.P., Acuña, M.H., Ness, N.F. Oxygen Auger electrons observed in Mars' ionosphere. Geophys. Res. Lett. 27, 1871–1874, 2000.

Molina-Cuberos, G.J., Lichtenegger, H., Schwingenschuh, K., López-Moreno, J.J., Rodrigo, R. Ion-neutral chemistry model of the lower ionosphere of Mars. J. Geophys. Res. 107, 5027, doi:10.1029/2000JE001447, 2002.

Molina-Cuberos, G.J., López-Moreno, J.J., Rodrigo, R., Lichtenegger, H., Schwingenschuh, K. A model of the martian ionosphere below 70 km. Adv. Space Res. 27, 1801–1806, 2001.

Molina-Cuberos, G.J., Witasse, O., Lebreton, J.-P., Rodrigo, R., López-Moreno, J.J. Meteoric ions in the atmosphere of Mars. Planet. Space Sci. 51, 239–249, 2003.

Morgan, D.D., Gurnett, D.A., Kirchner, D.L., Fox, J.L., Nielsen, E., Plaut, J.J. Variation of the martian ionospheric electron density from Mars Express radar soundings. J. Geophys. Res. 113, A09303, doi:10.1029/2008JA013313, 2008.

Morgan, D.D., Gurnett, D.A., Kirchner, D.L., Huff, R.L., Brain, D.A., Boynton, W.V., Acuña, M.H., Plaut, J.J., Picardi, G. Solar control of radar wave absorption by the martian ionosphere. Geophys. Res. Lett. 33, L13202, doi:10.1029/2006GL026637, 2006.

Morgan, D.D., Gurnett, D.A., Kirchner, D.L., Winningham, J.D., Frahm, R., Brain, D.A., Mitchell, D.L., Luhmann, J.G., Nielsen, E., Espley, J.R., Acuña, M.H., Plaut, J.J. Radar absorption due to a corotating interaction region encounter with Mars detected by MARSIS. Icarus, in press.

Nagy, A.F., Cravens, T.E. Solar system ionospheres, in: Mendillo, M., Nagy, A.F., Waite, J.H. (Eds.), Atmospheres in the Solar System: Comparative Aeronomy. American Geophysical Union, Washington, DC, pp. 39–54, 2002.

Nagy, A.F., Winterhalter, D., Sauer, K., Cravens, T.E., Brecht, S., Mazelle, C., Crider, D., Kallio, E., Zakharov, A., Dubinin, E., Verigin, M., Kotova, G., Axford, W.I., Bertucci, C., Trotignon, J.G. The plasma environment of Mars. Space Sci. Rev. 111, 33–114, 2004.

Ness, N.F., Acuña, M.H., Connerney, J.E.P., Kliore, A.J., Breus, T.K., Krymskii, A.M., Cloutier, P., Bauer, S.J. Effects of magnetic anomalies discovered at Mars on the structure of the martian ionosphere and solar wind interaction as follows from radio occultation experiments. J. Geophys. Res. 105, 15991–16004, 2000.

Nielsen, E., Fraenz, M., Zou, H., Wang, J.-S., Gurnett, D.A., Kirchner, D.L., Morgan, D.D., Huff, R., Safaeinili, A., Plaut, J.J., Picardi, G., Winningham, J.D., Frahm, R.A., Lundin, R. Local plasma processes and enhanced electron densities in the lower ionosphere in magnetic cusp regions on Mars. Planet. Space Sci. 55, 2164–2172, 2007a.

Nielsen, E., Morgan, D.D., Kirchner, D.L., Plaut, J., Picardi, G. Absorption and reflection of radio waves in the martian ionosphere. Planet. Space Sci. 55, 864–870, 2007b.

Nielsen, E., Wang, X.-D., Gurnett, D.A., Kirchner, D.L., Huff, R., Orosei, R., Safaeinili, A., Plaut, J.J., Picardi, G. Vertical sheets of dense plasma in the topside martian ionosphere. J. Geophys. Res. 112, E02003, doi:10.1029/2006JE002723, 2007c.

Nielsen, E., Zou, H., Gurnett, D.A., Kirchner, D.L., Morgan, D.D., Huff, R., Orosei, R., Safaeinili, A., Plaut, J.J., Picardi, G. Observations of vertical reflections from the topside martian ionosphere. Space Sci. Rev. 126, 373–388, 2006.

Nier, A.O., McElroy, M.B. Composition and structure of Mars' upper atmosphere — results from the neutral mass spectrometers on Viking 1 and 2. J. Geophys. Res. 82, 4341–4349, 1977.

Pätzold, M., Tellmann, S., Häusler, B., Hinson, D., Schaa, R., Tyler, G.L. A sporadic third layer in the ionosphere of Mars. Science 310, 837–839, 2005.

Pätzold, M., Withers, P., Tellmann, S.A., Mendillo, M., Peter, K., Häusler, B., Hinson, D.P., Tyler, G.L. The structure of the Mars ionosphere. AGU Fall Meeting Abstr. (P32A01), 2007.

Pesnell, W.D., Grebowsky, J. Meteoric magnesium ions in the martian atmosphere. J. Geophys. Res. 105, 1695–1708, 2000.

Picardi, G., Biccari, D., Seu, R., Plaut, J., Johnson, W.T.K., Jordan, R.L., Safaeinili, A., Gurnett, D.A., Huff, R., Orosei, R., Bombaci, O., Calabrese, D., Zampolini, E. MARSIS: Mars Advanced Radar for Subsurface and Ionosphere Sounding. ESA SP-1240: Mars Express: the Scientific Payload. Available from: <http://sci.esa.int/science-e/www/object/index.cfm?fobjectid=34885>, pp. 51–69, 2004.

Rishbeth, H., Garriott, O.K. Introduction to Ionospheric Physics. Academic Press, New York, 1969.

Rishbeth, H., Mendillo, M. Ionospheric layers of Mars and Earth. Planet. Space Sci. 52, 849–852, 2004.

Russell, C.T. Foreword. Space Sci. Rev. 126, 1–4, 2006.

Safaeinili, A., Kofman, W., Mouginot, J., Gim, Y., Herique, A., Ivanov, A.B., Plaut, J.J., Picardi, G. Estimation of the total electron content of the martian ionosphere using radar sounder surface echoes. Geophys. Res. Lett. 34, L23204, doi:10.1029/2007GL032154, 2007.

Schunk, R.W., Nagy, A.F. Ionospheres. Cambridge University Press, New York, 2000.

Shinagawa, H. Our current understanding of the ionosphere of Mars. Adv. Space Res. 26, 1599–1608, 1996.

Shinagawa, H., Cravens, T.E. A one-dimensional multispecies magneto-hydrodynamic model of the dayside ionosphere of Mars. J. Geophys. Res. 94, 6506–6516, 1989.

Shinagawa, H., Cravens, T.E. The ionospheric effects of a weak intrinsic magnetic field at Mars. J. Geophys. Res. 97, 1027–1035, 1992.

Stewart, A.I.F., Alexander, M.J., Meier, R.R., Paxton, L.J., Bougher, S.W., Fesen, C.G. Atomic oxygen in the martian thermosphere. J. Geophys. Res. 97, 91–102, 1992.

Trotignon, J.G., Parrot, M., Cerisier, J.C., Menvielle, M., Axford, W.I., Paëtzold, M., Warnant, R., Wernik, A.W. The plasma environment of Mars: from the shocked solar wind down to the ionosphere. Planet. Space Sci. 48, 1181–1191, 2000.

Tyler, G.L., Balmino, G., Hinson, D.P., Sjogren, W.L., Smith, D.E., Simpson, R.A., Asmar, S.W., Priest, P., Twicken, J.D. Radio science observations with Mars Global Surveyor: orbit insertion through one Mars year in mapping orbit. J. Geophys. Res. 106, 23327–23348, 2001.

Tyler, G.L., Balmino, G., Hinson, D.P., Sjogren, W.L., Smith, D.E., Woo, R., Asmar, S.W., Connally, M.J., Hamilton, C.L., Simpson, R.A. Radio science investigations with Mars Observer. J. Geophys. Res. 97, 7759–7779, 1992.

Wang, J.-S., Nielsen, E. Wavelike structures in the martian topside ionosphere observed by Mars Global Surveyor. J. Geophys. Res. 108, 5078, doi:10.1029/2003JE002078, 2003.

Winchester, C., Rees, D. Numerical models of the martian coupled thermosphere and ionosphere. Adv. Space Res. 15 (4), 51–68, 1995.

Withers, P. Mars Global Surveyor and Mars Odyssey accelerometer observations of the martian upper atmosphere during aerobraking. Geophys. Res. Lett. 33, L02201, doi:10.1029/2005GL024447, 2006.

Withers, P. Variability in the ionosphere of Mars. COSPAR Meeting (C32–0011–0008), 2008.

Withers, P., Bougher, S.W., Keating, G.M. The effects of topographically-controlled thermal tides in the martian upper atmosphere as seen by the MGS accelerometer. Icarus 164, 14–32, 2003.

Withers, P., Mendillo, M. Response of peak electron densities in the martian ionosphere to day-to-day changes in solar flux due to solar rotation. Planet. Space Sci. 53, 1401–1418, 2005.

Withers, P., Mendillo, M., Hinson, D. Space weather effects on the Mars ionosphere due to solar flares and meteors, in: European Planetary Science Congress. EPSC2006-A-00190, 2006.

Withers, P., Mendillo, M., Hinson, D.P., Cahoy, K. Physical characteristics and occurrence rates of meteoric plasma layers detected in the martian ionosphere by the Mars Global Surveyor Radio Science Experiment. J. Geophys. Res. 113, A12314, 110.1029/2008JA013636, 2008.

Withers, P., Mendillo, M., Pätzold, M., Tellmann, S., Christou, A.A., Vaubaillon, J. Comparison of seasonal variations in the meteoric layer of the martian ionosphere and predicted meteor showers. Icarus, under review.

Withers, P., Mendillo, M., Rishbeth, H., Hinson, D.P., Arkani-Hamed, J. Ionospheric characteristics above martian crustal magnetic anomalies. Geophys. Res. Lett. 32, L16204, doi:10.1029/2005GL023483, 2005.

Woods, T.N., Kopp, G., Chamberlin, P.C. Contributions of the solar ultraviolet irradiance to the total solar irradiance during large flares. J. Geophys. Res. 111, A10S14, doi:10.1029/2005JA011507, 2006.

Zhang, M.H.G., Luhmann, J.G., Kliore, A.J. An observational study of the nightside ionospheres of Mars and Venus with radio occultation methods. J. Geophys. Res. 95, 17095–17102, 1990a.

Zhang, M.H.G., Luhmann, J.G., Kliore, A.J., Kim, J. A post-Pioneer Venus reassessment of the martian dayside ionosphere as observed by radio occultation methods. J. Geophys. Res. 95, 14829–14839, 1990b.

Zou, H., Wang, J.-S., Nielsen, E. Reevaluating the relationship between the martian ionospheric peak density and the solar radiation. J. Geophys. Res. 111, A07305, doi:10.1029/2005JA011580, 2006.